

RADIATIVE MUON CAPTURE ON NUCLEAR TARGETS

by

ALVARO SERNA

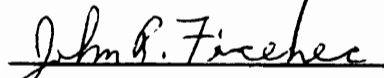
Dissertation submitted to the Faculty of the
Virginia Polytechnic Institute and State University
in partial fulfillment of the requirements for the degree of

DOCTOR OF PHILOSOPHY

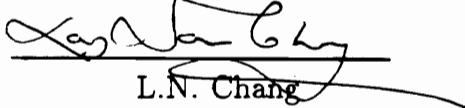
in
Physics

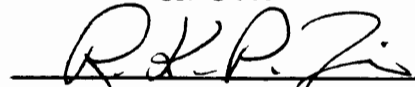
APPROVED:


M. Blecher, Chairman


J. Ficenech


K. Gotow


L.N. Chang


R.P.K. Zia

October 1991

Abstract

A large acceptance pair spectrometer to detect photons from the radiative muon capture (RMC) process was built. The spectrometer was used to measure the RMC branching ratio for **Al, Si, Ca, Mo, Sn** and **Pb**. Two recent theoretical models were used to extract the RMC branching ratio in Ca. The experimental **result** is in good agreement with the world average value, but yields a value for the pseudoscalar coupling constant, g_p , which is lower than the Goldberger-Treiman PCAC prediction. In the absence of a theoretical model to predict the RMC rates for Al and Si, only the branching ratios for these targets are reported. For Mo, Sn, and Pb, the branching ratios found were consistent with the Fermi gas model for which a null contribution from the pseudoscalar coupling was assumed. Good agreement was found between the experimental results and what is predicted from using the simple, closure approximation.

The RMC world data indicates a close connection between the branching ratios and α , where α is the ratio between the difference and the sum of neutrons and protons for any element, ($\alpha = \frac{(N-Z)}{(N+Z)}$). It is suggested that future experiments study different isotopes to isolate the Z and the α dependence of the RMC rates.

This experiment also served as a test ground for the RMC experiment in liquid hydrogen which is now in progress at TRIUMF.

Acknowledgements

This work could not had been completed without the continuous help I received from Dr. David S. Armstrong. I learnt most from his answers to my countless questions. His friendship and great knowledge of the field, are highly regarded and appreciated. I am also in great debt to all the RMC group members who helped in all the different aspects of this experiment.

I would also like to thank my advisor, Dr. Marvin Blecher, for accepting and trusting me as his student. I am also thankful to all the staff at the Physics Department for their permanent support.

Finally, I would like to thank my wife who gave me the two most wonderful daughters during my graduate years, made innumerable sacrifices for me, and still loves me and is willing to keep me as her husband.

Contents

| | | |
|----------|---|-----------|
| 1 | Introduction | 1 |
| 1.1 | Motivation | 1 |
| 1.2 | Partially Conserved Axial-Vector Current (PCAC) | 3 |
| 1.3 | The Induced Pseudoscalar Coupling | 5 |
| 1.3.1 | Ordinary Muon Capture | 6 |
| 1.3.2 | Radiative Muon Capture | 7 |
| 2 | Theory | 8 |
| 2.1 | Radiative Muon Capture | 8 |
| 2.2 | The Elementary Amplitude | 8 |
| 2.3 | Elementary-Particle Approach to Nuclear RMC | 9 |
| 2.4 | Impulse Approximation | 9 |
| 3 | The RMC Detector | 15 |
| 3.1 | The Drift Chamber | 16 |
| 3.1.1 | Construction | 16 |
| 3.1.2 | Performance | 24 |
| 3.2 | Inner Wire Chamber | 30 |
| 3.3 | The Magnet | 32 |
| 3.4 | Targets | 32 |
| 3.5 | Beamline | 34 |
| 3.6 | Cosmic Counters | 35 |

| | | |
|----------|---|-----------|
| 3.7 | Trigger Scintillators | 35 |
| 4 | Data Analysis | 37 |
| 4.1 | Introduction | 37 |
| 4.2 | Track Reconstruction | 38 |
| 4.2.1 | Transverse momentum | 38 |
| 4.2.2 | Longitudinal momentum | 39 |
| 4.2.3 | Software Cuts | 40 |
| 4.3 | Monte Carlo | 45 |
| 4.4 | Corrections, backgrounds | 49 |
| 4.4.1 | Counting the captured muons | 49 |
| 4.4.2 | Counting photons | 51 |
| 4.4.3 | Errors | 53 |
| 4.5 | Branching Ratios | 56 |
| 4.5.1 | ^{27}Al , ^{28}Si | 57 |
| 4.5.2 | ^{40}Ca | 58 |
| 4.5.3 | Mo, Sn and Pb | 59 |
| 5 | Results and Conclusions | 73 |
| 5.1 | Results | 73 |
| 5.1.1 | Al, Si | 73 |
| 5.1.2 | ^{40}Ca | 74 |
| 5.1.3 | Mo, Sn Pb | 76 |
| 5.2 | Summary of RMC results | 78 |
| 5.3 | Suggestions for further work | 79 |

Bibliography

81

Vitae

84

List of Tables

| | | |
|-----|---|----|
| 1.1 | Summary of measurements of OMC in hydrogen | 6 |
| 3.1 | Detector dimensions | 20 |
| 3.2 | Wires and tensions used | 21 |
| 3.3 | Dimensions of the targets used | 34 |
| 4.1 | Tracking cuts used in the analysis | 43 |
| 4.2 | Effect of prompt cuts | 45 |
| 4.3 | Lifetimes and Huff factors | 51 |
| 4.4 | Different data corrections | 53 |
| 4.5 | Contributions to the error in the branching ratio | 56 |
| 4.6 | Branching ratios for aluminum and silicon | 58 |
| 4.7 | Branching ratios for ^{40}Ca | 59 |
| 4.8 | RMC branching ratios for Mo, Sn and Pb | 61 |
| 5.1 | Summary of RMC results for ^{40}Ca from recent measurements. | 75 |
| 5.2 | Branching ratios using Christillin's closure approximation | 77 |
| 5.3 | Summary of RMC branching ratios for $\alpha = 0$ nuclei | 79 |

List of Figures

| | | |
|-----|--|----|
| 2.1 | Feynman diagrams contributing to RMC | 10 |
| 3.1 | Global view of the RMC Detector | 17 |
| 3.2 | XY view of a typical event | 18 |
| 3.3 | Drift chamber cell geometry | 22 |
| 3.4 | Drift chamber efficiency | 25 |
| 3.5 | Benefits of staggering the sense wires | 27 |
| 3.6 | Time resolution | 28 |
| 3.7 | RZ view of an event | 31 |
| 3.8 | IWC wire crossings | 33 |
| 4.1 | Drift distance | 41 |
| 4.2 | High energy tail | 42 |
| 4.3 | Energy spectrum for RMC in lead | 62 |
| 4.4 | Prompt rejection | 63 |
| 4.5 | Probability of photoconversion in lead | 64 |
| 4.6 | Trigger efficiency | 64 |
| 4.7 | Energy resolution at 129.4 MeV | 65 |
| 4.8 | Energy resolution for 80 MeV photons | 65 |

| | | |
|------|---|----|
| 4.9 | Radiative pion capture in carbon | 66 |
| 4.10 | Bound muon lifetime in Si | 66 |
| 4.11 | Muon lifetime in lead and tin | 67 |
| 4.12 | Typical input and folded spectra | 68 |
| 4.13 | Comparison between polynomial and aluminum data | 69 |
| 4.14 | Comparison between polynomial and silicon data | 69 |
| 4.15 | Comparison between Gmitro's theory and Ca data | 70 |
| 4.16 | Comparison between Christillin's theory and Ca data | 70 |
| 4.17 | Comparison between Christillin's theory and Pb data | 71 |
| 4.18 | Comparison between Christillin's theory and Sn data | 71 |
| 4.19 | Comparison between Christillin's theory and Mo data | 72 |
| 5.1 | $N_{\geq 57}^{\gamma}$ from ^{40}Ca as a function of g_p/g_a for the theories of Christillin [1] and Gmitro <i>et al.</i> [2] | 76 |
| 5.2 | Comparison between branching ratios for this work and those of Döbeli <i>et al.</i> [3] as a function of Z | 79 |
| 5.3 | Comparison between branching ratios for this work and those of Döbeli <i>et al.</i> [3] as a function of α | 80 |

Chapter 1

Introduction

1.1 Motivation

Since the early years of nuclear physics research it has been observed that some nuclei spontaneously decay and emit electrons or positrons. This process is known as beta decay. The first comprehensive theory to explain this nuclear transition process was put forward in 1934 by Fermi [4]. He noted that beta decay was a novel interaction; shorter in range than the strong interaction among nucleons, and weaker in strength than the electromagnetic interaction. Fermi based his theory on the very successful theory of quantum electrodynamics, and assumed a vector interaction among four fermions involved in the decay, taking place at a single point. This four-fermion interaction was very successful in explaining weak processes.

In 1936 the muon was discovered in cosmic rays, and it was soon realized that muon decay, a pure weak decay in which strongly interacting particles do not participate, could be explained by the weak interaction theory as a four fermion point interaction. Fermi's theory was expanded to include the muon interactions.

However, in addition to the vector interaction, it was found that an axial vector interaction also contributes to weak interaction processes. A theory emerged, called V-A, that treated the interaction as the difference between vector and axial vector currents, which satisfied the experimental results available. Muon decay experiments served as a laboratory to test the V-A theory.

In the late 1960's, a comprehensive theory of the weak and electromagnetic interactions was presented by Glashow, Weinberg and Salam [5,6,7]. This theory is now known as the standard model because it has been so successful in accounting for experimental results.

However, there are still unsolved questions about weak interactions at low energies. In a semileptonic process, i.e. a process that involves leptons (electrons and muons) and strongly interacting particles, the strong interactions induce extra couplings. One of these couplings, the pseudoscalar, is poorly known. The most sensitive ways to probe the pseudoscalar interaction are through muon capture experiments. Ordinary muon capture (OMC) is the process $\mu^- N(A, Z) \rightarrow N(A, Z - 1)\nu$. When a muon is stopped in matter it forms a muonic atom and cascades quickly ($\sim 10^{-13}$ s) down to the 1S orbit. For a large Z nuclei, like lead, a naive first estimate of the 1S state radius of the muonic atom is ~ 3 fm. For this same nucleus the half density radius is ~ 6.5 fm. It is then clear that for such a muonic atom the wave function overlap between the muon and the nucleus is sufficiently large to make muon capture compete with the muon decay. In OMC, the pseudoscalar coupling makes an important contribution to the total capture rate. However, in OMC the momentum transfer is fixed due to the two body final state. The radiative muon capture process (RMC), $\mu^- N(A, Z) \rightarrow N(A, Z - 1)\nu\mu\gamma$, allows for a large range of momentum transfer making its rate more sensitive to the pseudoscalar coupling strength.

Besides the muon capture process, the induced pseudoscalar coupling also contributes to other processes such as beta decay. However the contribution depends on the momentum transfer (see equations 1.4 and 1.5), which is relatively small for beta decay. As a consequence very little has been learned about the pseudoscalar

coupling from this process.

This thesis describes an RMC experiment in which the gamma spectrum and the branching ratio were measured in six different targets (Al, Si, Ca, Mo, Sn and Pb). From the analysis of these quantities a value of g_p , the pseudoscalar coupling constant, was extracted.

1.2 Partially Conserved Axial-Vector Current (PCAC)

The value of g_p can be predicted from general field theory methods and the assumption of PCAC [8]. The Lagrangian that represents the semileptonic interaction is formed as a current-current interaction similar to the one proposed by Fermi,

$$\mathcal{L}_{eff}(x) = -\frac{G_F}{2} J_\lambda^\dagger(x) J^\lambda(x) + h.c. \quad (1.1)$$

where G_F is the Fermi coupling constant, and the current J^λ is broken into a hadronic (strong) and a leptonic part

$$J_\lambda(x) = J_\lambda^h + J_\lambda^l. \quad (1.2)$$

The hadronic part of the interaction is responsible for the induced couplings, g_p being one of them.

The hadronic current is decomposed in two parts with different transformation properties,

$$J_\lambda^h = \cos \theta_c (V_\lambda - A_\lambda) \quad (1.3)$$

with

$$V_\lambda = i\bar{u}_p [f_v(q^2)\gamma_\lambda + f_m(q^2)\sigma_{\lambda\nu}q_\nu] u_n \quad (1.4)$$

$$A_\lambda = -\bar{u}_p [f_a(q^2)\gamma_\lambda\gamma_5 + if_p(q^2)\gamma_5q_\lambda] u_n \quad (1.5)$$

where θ_c is the Cabbibo angle, that broadly speaking accounts for the fact that strangeness changing decays appear to be weaker than strangeness nonchanging decays, and q is the momentum transfer. Possible scalar and tensor form factors have been dropped because of lack of experimental evidence for them. The terms f_v and f_a are the vector and axial vector form factors. The weak magnetic f_m and the pseudoscalar form factors f_p are induced by the strong interaction.

The assumption that the axial current is conserved, and use of the current-current interaction will lead to the unphysical result that the pion mass is zero and/or that the pion will not decay. Thus the hypothesis that the axial current is partially conserved is employed. This means that conservation is recovered in the limit that the pion mass is zero. Thus the divergence of the axial current is written,

$$\partial_\lambda A_\lambda = f_\pi m_\pi^2 \phi_\pi \quad (1.6)$$

where f_π is the pion decay constant, m_π is the pion mass and ϕ_π is the pion field. If the matrix element between two nucleon states is formed,

$$\langle u_p(k') | A_\mu | u_n(k) \rangle = \bar{u}_p(k') \left[\gamma_\mu \gamma_5 f_a(q^2) + q_\mu \gamma_5 f_p(q^2) \right] u_n(k). \quad (1.7)$$

The divergence of this current is:

$$\langle u_p(k') | \partial^\mu A_\mu | u_n(k) \rangle = i \bar{u}_p(k') \gamma_5 u_n(k) \left[2M_N f_a(q^2) + q^2 f_p(q^2) \right]. \quad (1.8)$$

Using PCAC the divergence can also be written:

$$\langle u_p(k') | \partial^\mu A_\mu | u_n(k) \rangle = \frac{2f_\pi m_\pi^2}{q^2 + m_\pi^2} g_{\pi NN}(q^2) i \bar{u}_p(k') \gamma_5 u_n(k), \quad (1.9)$$

where $g_{\pi NN}$ is the pion nucleon coupling constant. Comparing the last two results yields:

$$\frac{2f_\pi m_\pi^2}{q^2 + m_\pi^2} g_{\pi NN}(q^2) = 2M_N f_a(q^2) + q^2 f_p(q^2). \quad (1.10)$$

If $q^2 = 0$

$$f_\pi g_{\pi NN}(0) = M_N f_a(0) \quad (1.11)$$

so that assuming a small variation of f_a and $g_{\pi NN}$ from $q^2 = 0$ to $q^2 = m_\pi^2$ yields,

$$f_a = \frac{f_\pi g_{\pi NN}}{M_N}, \quad (1.12)$$

which is known as the Goldberger-Treiman relation.

At the pion pole

$$f_p(q^2) = \frac{2M_N}{m_\pi^2 + q^2} f_a(0) \quad (1.13)$$

In terms of the pseudoscalar coupling constant in μ capture, defined as $g_p = m_\mu f_p$ and $g_a = f_a$,

$$g_p = \frac{2M_N m_\mu g_a}{m_\pi^2 + q^2} \quad (1.14)$$

For OMC on a proton, $\mu^- p \rightarrow n \nu$, $q^2 = 0.88m_\mu^2$ and

$$g_p = 6.78g_a. \quad (1.15)$$

So, a measurement of g_p is a test of PCAC.

1.3 The Induced Pseudoscalar Coupling

Once a muon is stopped, the capture probability by a nucleus obviously increases with the atomic number Z . For hydrogen the capture to decay ratio is $\sim 4 \times 10^{-4}$ while for $Z=50$ this same ratio is ~ 25 . Because of this small branching ratio for hydrogen, most efforts, including this one, have concentrated on the nuclear muon capture process. The extraction of g_p from a nuclear capture process has the difficulty of understanding how the muon-proton interaction gets affected by the surrounding nucleons. In other words if one is interested in one pion exchange processes, when in a large nucleus the pion will scatter on the surrounding nucleons

Table 1.1: Summary of values of g_p and g_p/g_a as determined from measurements of OMC on hydrogen. The values presented are from the analysis of Bardin *et al.* [9]

| Reference | Target | g_p | g_p/g_a |
|------------------------------------|-----------------------|----------------|---------------|
| Bleser et al. 1962 [10] | liquid H ₂ | 6.0 ± 8.0 | 4.8 ± 6.3 |
| Rothberg et al. 1963 [11] | liquid H ₂ | 11.0 ± 4.3 | 8.7 ± 3.4 |
| Alberigi Quaranta et al. 1969 [12] | gas H ₂ | 10.3 ± 3.9 | 8.2 ± 3.1 |
| Bystritskii et al. 1974 [13] | gas H ₂ | 7.9 ± 5.9 | 6.3 ± 4.7 |
| Bardin et al. 1981 [14] | liquid H ₂ | 7.1 ± 3.0 | 5.6 ± 2.4 |
| Average | | 8.7 ± 1.9 | 6.9 ± 1.5 |

which will act as source of virtual pions. The pion field ϕ_π^m of the medium will have to be modified as compared to the free pion field. In addition, when calculating nuclear transitions to different energy levels one will need to know the nuclear wave functions fairly well to extract g_p from the RMC energy spectrum.

1.3.1 Ordinary Muon Capture

Information about g_p can be obtained in OMC by measuring the muon capture rate in hydrogen. Though these experiments are difficult because of the necessity to accurately measure the neutron spectrum, several have been carried out. A summary of the results is presented in Table 1.1. They agree with the Goldberger-Treiman value for g_p although the errors are large. Most of the early experiments were designed to test the spin dependence of the muon capture reaction. This in turn was a test of the now well accepted V-A weak interaction theory.

A few experiments have extracted g_p from OMC in nuclear targets (¹⁶O, ¹²C and ²⁸Si), in some cases giving a value higher than that predicted by the Goldberger-Treiman relation. These conclusions, however, are not definitive due to the uncertainties in the nuclear physics calculations.

1.3.2 Radiative Muon Capture

As previously discussed, in OMC the momentum transfer is fixed while in RMC (three particles in final state) the momentum transfer can vary. In the case of RMC on a proton q^2 varies from $0.88m_\mu^2$ to $-1.0m_\mu^2$. This makes the RMC rate much more sensitive to g_p . Another advantage in the RMC experiments is that it is easier to measure the energy of gamma rays than it is to detect neutrons. These advantages outweigh the fact that RMC is a rare process; the branching ratio RMC/OMC is of the order of 10^{-5} .

RMC on hydrogen presents the cleanest reaction for the extraction of g_p . A spectrometer, to be described in chapter 3, was constructed at TRIUMF to measure this reaction. In order to test the spectrometer under realistic conditions it was decided to study the higher rate RMC process on nuclei. The latter process is interesting in its own right. Previous data, to be reviewed in chapter 5, indicated that for light nuclei g_p is renormalized upwards while in heavy nuclei g_p is renormalized downwards. The heavy nuclear data is old and suspect. Extracting g_p in nuclear RMC depends on the quality of the nuclear theory, described in chapter 2. In this experiment capture rates on six nuclear targets: Al, Si, Ca, Mo, Sn, and Pb were measured and the methods of analysis are presented in chapter 4.

Chapter 2

Theory

2.1 Radiative Muon Capture

Since Rood and Tolhoek [15] pointed out that RMC was especially sensitive to g_p , there has been a considerable effort to calculate this process. Before calculating muon capture on nuclei one should first understand the capture on a free proton. Several different approaches to calculate this elementary amplitude have been used. They all agree fairly well, indicating that this elementary process is well understood. In calculating the nuclear rates one must use the elementary amplitude but also introduce possible modifications due to surrounding nucleons. In addition, information on the final state nuclear wave functions is required. For a detailed review see Gmitro and Truöl [16].

2.2 The Elementary Amplitude

One approach to calculate the elementary amplitude is to evaluate the diagrams in Figure 2.1. These terms represent radiation from: the muon, the charge and magnetic moment of the proton, the magnetic moment of the neutron and from the charge of the pion exchanged. The extra diagrams are included to restore gauge invariance.

A different method, based on current divergence, was used by Christillin and Servadio [17]. Both calculations are in agreement.

By using conservation of the electromagnetic current, vector current conser-

vation (CVC) and PCAC, Hwang and Primakoff [18,19] attempted a more general calculation of the elementary amplitude. However, an additional assumption was needed that fixed the functional dependence of the form factors. When considering one pion exchange the q^2 dependence of the pseudoscalar form factor was not included. This was recognized and fixed quickly [20,21,22], recovering the usual amplitude.

Finally, a fully relativistic calculation that also includes possible contributions due to the $\Delta(1232)$ resonance was carried out by Beder and Fearing [23]. They find an 8% enhancement for the high energy region of the gamma spectrum for RMC on the proton. However it is not clear what these corrections should be for nuclear capture.

2.3 Elementary-Particle Approach to Nuclear RMC

One approach to calculating the nuclear RMC amplitude is to consider the nucleus as an elementary, structureless, particle. In the elementary particle model (EPM), [21,22], form factors are introduced as properties of the nucleus. This alone makes this method unreliable since all form factors involved display a strong q^2 dependence. Furthermore, in the EPM it is difficult to include intermediate excited states which contribute to the RMC amplitude. Because of these problems different methods will be used to interpret the data obtained in this experiment.

2.4 Impulse Approximation

As a first approach to calculate how a muon captured by a nucleus is affected by the individual nucleons one could take each individual muon-nucleon interaction and sum over all nucleons. This impulse approximation (IA) ignores possible effects

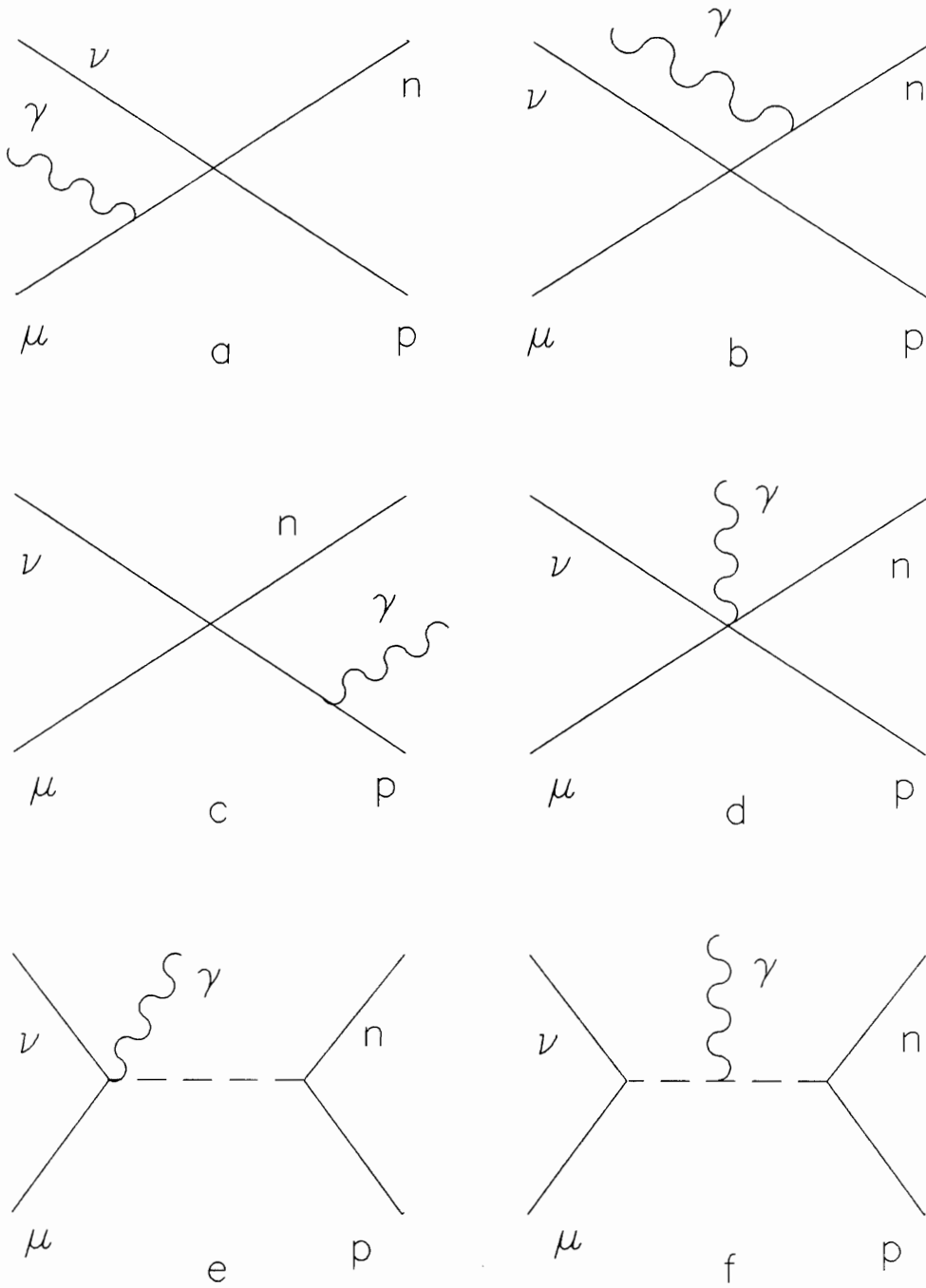


Figure 2.1: Feynman diagrams contributing to RMC

due to nucleon-nucleon interactions and uses the free weak coupling constants for each nucleon. Since the nucleon-nucleon interaction does play an important role in the RMC amplitude a modification of the IA is needed to include mesonic effects. Instead of using the free couplings for the nucleons, mesonic effects were introduced by using renormalized weak couplings [24]. Some useful conclusions were drawn from these studies: First the shape of the RMC spectrum was not very sensitive to g_p , second the RMC rate is strongly dependent on g_p , and third by using the same wave functions for RMC and OMC the RMC to OMC ratio proved to be not very sensitive to the particular wave functions used. However, replacing all the weak couplings by renormalized values ignores the individual q^2 dependence of these couplings.

Achmedov *et al.* [25] divides the mesonic effects into two classes. One pion exchange contributions are calculated explicitly. Many pion and heavier meson contributions are introduced via local effective charges. All the weak form factors, except the induced pseudoscalar, are local and can be described by effective charges. The induced pseudoscalar was treated independently. They found a 10-12% reduction in RMC/OMC for ^{40}Ca , which came closer to the experimental data, as compared to early calculations that used constant, average, coupling constants. Gmitro *et al.* [2] modified the impulse approximation by including mesonic effects connected to the electromagnetic vertex. They assume that a nuclear transition operator can be expressed fully in terms of a nuclear charge distribution. By imposing a continuity-equation constraint on the electric current and the charge density they achieve large reductions in the RMC rates. Radiative capture rates and the photon spectra for ^{16}O and ^{40}Ca were analysed by using the nuclear shell-model wave functions for the calculation of the partial RMC transition rates. Their results for

^{40}Ca are in agreement with Achmedov's. The ^{40}Ca data from this experiment will be compared to their results.

Christillin *et al.*[26] used the Fermi gas model to calculate the nuclear response function for medium and heavy nuclei ($Z \geq 42$). In the Fermi gas model it is assumed that all the nucleon momentum states, up to the Fermi momentum k_F , are filled, and no higher states are excited. They include in their treatment most physical aspects considered by Gmitro. The nuclear effects are included as corrections to the electromagnetic and weak vector currents. The main contribution of the weak vector current's matrix elements are expressed as multipoles of the charge distribution, and nucleonic values of the coupling constants are used. The only phenomenological parameter of the theory is an effective nucleon mass which value ($M^*=0.5 M$) is found by fitting predicted OMC rates to the experimental data. The observed suppression of the capture rates for heavy nuclei is introduced through a factor $(1 - \delta(N - Z)/A)$ where $\delta \sim 2.5$. To test their method, experimental OMC rates for 51 nuclei were compared to their predictions. Most values were off by less than 10%. Then RMC spectrums for a few nuclei were computed (Mo, Sn, Gd, W, Pb, and U).

More recently Fearing and Welsh (unpublished) performed a Fermi gas calculation, similar to that of Christillin, in the relativistic case. From relativistic mean field theory arguments, they derive the nucleon effective mass. In field theory the effects of the nuclear medium are described by scalar and vector mean fields. The effect of these potentials are equivalent to using, in the free nucleon equation, a renormalized nucleon mass. They find a value of $M^* \approx 0.57$. In their Fermi gas model calculation, different neutrino momenta for neutrons and protons is used. These momenta are taken as proportional to the cubic root of the respective nu-

cleon densities. Two different calculations are reported: one for a uniform, the other for a radially-varying density distribution. Leaving M^* as a free parameter, they fit its value by adjusting their predictions to the observed OMC rates. A value of $M^* = 0.529M$ was found for the uniform density distribution and their OMC as well as the RMC rates calculated agree very well with Christillin's. For the realistic density distribution the predicted OMC rates diverge from the observed values and large RMC/OMC discrepancies were obtained. The data for Mo, Sn and Pb will be compared to Christillin's prediction.

The Fermi gas model used for heavy nuclei cannot be extended either to light nuclei, or to nuclei with $N = Z$. Christillin [1] uses, for ^{40}Ca , a phenomenological approach to calculating the nuclear final states. In his inclusive calculation which sums over final states, the excitation spectrum depends on energy and momentum transfer, unlike the closure approximation where a mean excitation energy is assumed. The strength of the nuclear excitation energy is divided between giant dipole resonances (GDR) and higher states. The GDR, collective nuclear excitation where all the protons in the nucleus move together against all the neutrons, is approximately reproduced by a Lorentzian shape multiplied by the square of the elastic form factor of the ^{40}Ca ground state. This Lorentzian is taken at 20 MeV excitation energy with a 5 MeV width. Higher resonances can be understood as collective motion of protons with spin up together with neutrons with spin down, against the remaining protons with spin down and neutrons with spin up. For higher resonances, a Lorentzian at 35 MeV and 12 MeV width is used to account for the isovector quadrupole and monopole excitations. This procedure was also used in calculating the gamma spectrum from radiative pion capture in ^{12}C and has been confirmed from comparison with the experiment. The strength of both

spectrum contributions were adjusted to reproduce the ordinary capture rate. We will compare our data to their predicted values as well as to the recent experimental results of Armstrong *et al.* [27].

There are no calculations for Al and Si and the Fermi gas model results cannot be extrapolated from heavy to light nuclei. For these two nuclei the spectrum and total RMC/OMC ratios will be reported but a value of g_p cannot be extracted. One hopes the results presented will spark some interest in theoretical calculations for these two nuclei.

Chapter 3

The RMC Detector

The RMC detector was designed to study the gamma-ray spectrum from the radiative muon capture process. These gamma rays cover the 57 to 100 MeV energy region. In this energy region the following are the most important backgrounds that can contribute to the spectrum:

- **Bremsstrahlung of decay electrons from muons that stop in the target:** Although the expected maximum energy for this process should not exceed 52.5 MeV, poor energy resolution produces a spectrum beyond this limit.
- **Pion Capture:** Since the muons are produced from pion decays a large number of pions can and do make it to the target. Since nearly all pions are captured, their possible contribution to the gamma spectrum is large and peaks around 100 MeV.
- **Cosmic Rays:** Since their energy spectrum is wide and the only shielding of the detector is the magnet's yoke, cosmic rays represent a high fraction of the events seen by the detector.

In addition, as the RMC process is one of low rate a detector with large acceptance is required. With these facts in mind a pair spectrometer with a large acceptance centered around a multiwire cylindrical drift chamber was built to fulfill the following requirements :

- Measurement of the momenta of charged particles with high precision over a large solid angle.
- Identification and rejection of events other than photons coming from muon capture in the target.

The following detector components will be described: drift chamber and multiwire proportional chamber for tracking, scintillators for triggering, lead converter for pair production, spectrometer magnet, cosmic-ray veto scintillators and wire chambers, and targets. In addition a radio frequency separator (RFS) located in the beam line and essential for pion contamination suppression will be discussed. A global view of the whole detector is shown in Figure 3.1. Detector dimensions are found in Table 3.1. Figure 3.2 shows the XY projection of a typical reconstructed track, and the corresponding scintillators that fired.

3.1 The Drift Chamber

The heart of the spectrometer is the multiwire cylindrical drift chamber. The Drift Chamber was designed to have a position resolution of $150\mu\text{m}$, an energy resolution of 12% for 129 MeV photons and a solid angle of $\sim 2\pi$. The chamber was segmented in four layers, with one layer wired in stereo. A gas mixture with a drift velocity of $50\mu\text{m}/\text{nsec}$ was chosen. The chamber was designed to operate in an axial magnetic field.

3.1.1 Construction

General Machining The RMC drift chamber consists basically of two aluminum endplates held together by inner and outer carbon fiber cylindrical walls. Insulating feedthrus were glued through slots on the endplates. All the wires are strung from

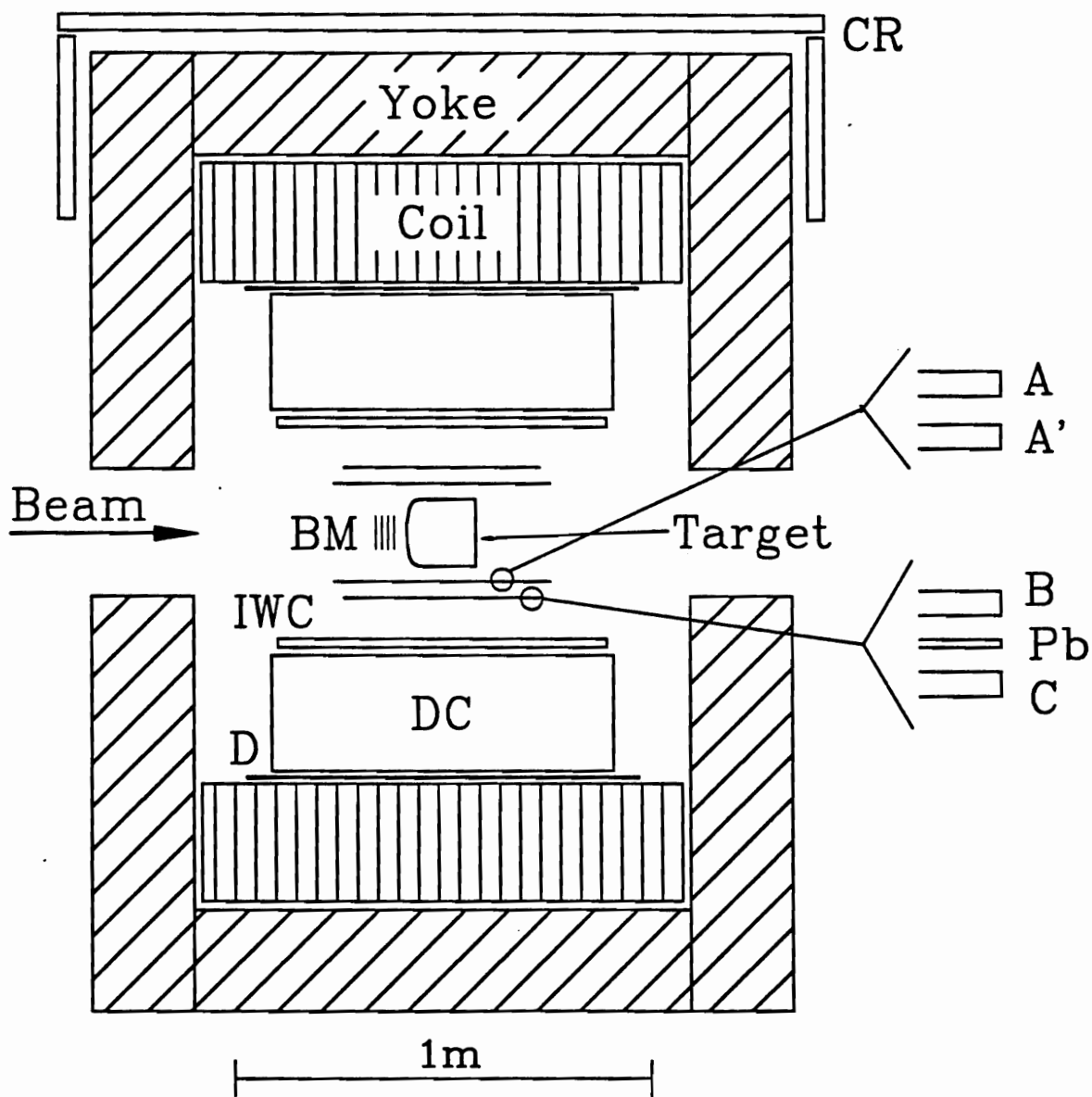
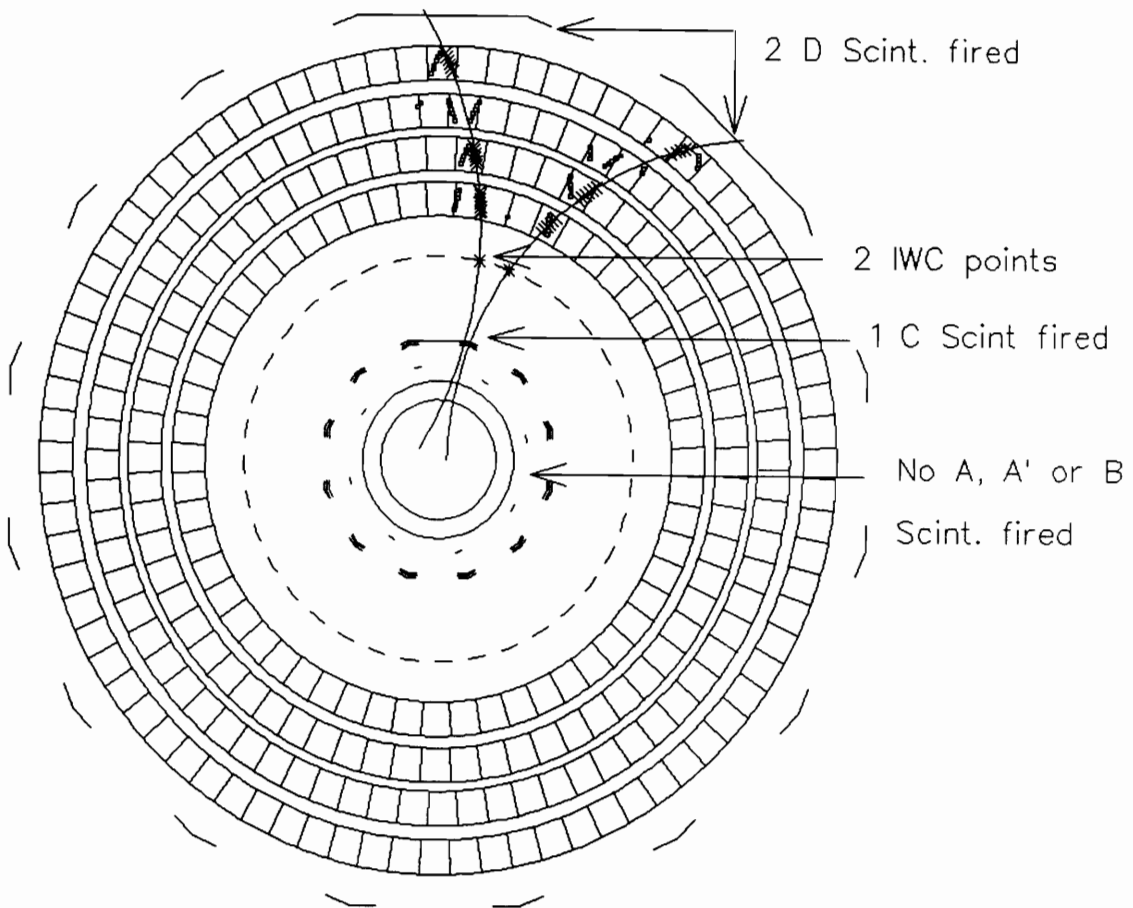


Figure 3.1: Global view of the RMC detector



| | |
|-------|-----|
| RUN | 718 |
| EVENT | 2 |

Figure 3.2: XY view of a pair

one end to the other of the drift chamber through holes in these feedthrus. The endplate slots were measured to have been machined to a $75\mu\text{m}$ precision with respect to the ideal designed positions. The endplates had inner and outer radii of 30.2 cm and 50.8 cm and a thickness of 0.95 cm, and were pre-stressed by a series of rods that at the end of the stringing were removed and replaced by the outer carbon fiber. The slots for layer three were machined at an angle of 7° with respect to the axial direction to match the stereo angle of stringing for this layer.

Injection-molded noryl feedthrus were used to position the wires in the endplates. After a two month period of curing, these feedthrus proved to be good insulators, and to show negligible deformation in the temperature range 10° to 40° C. Three different jigs to drill the holes in the feedthrus were made : one for the cathodes, and since the anodes were staggered, a different one for the anodes of each plate. The holes in the jigs were drilled to a precision of $25\mu\text{m}$ with respect to each other as compared to the ideal designed position. After drilling, a sample of 100 feedthrus were measured. The standard deviation of the gaussian distribution of the hole positions with respect to the jigs were measured to be $20\mu\text{m}$ for the cathodes, $35\mu\text{m}$ for the upstream plate and $45\mu\text{m}$ for the downstream plate. The holes, however, were not centered with respect to the slots in either the radial or the angular position. This implied that after gluing, the holes of one side were shifted radially with respect to the holes of the other side by $75\mu\text{m}$. In the angular direction this shift was almost negligible. All the feedthrus were visually scanned, hand cleaned and only those that fitted tightly on the slots were glued to the endplates.

The two endplates were glued to the inner carbon fiber cylinder, and held apart by tension rods. Before stringing the alignment of one plate with respect to the other was measured. The position of the slots on one plate with respect to the

Table 3.1: Detector dimensions

| Item | | Radius | Comments |
|--|--------------|---------------|------------------|
| Veto A Scint. | 4 Arcs | 12.20 | 508x3.2 mm |
| Veto A' Scint. | 4 Arcs | 12.60 | 508x3.2 mm |
| Veto B Scint | 12 Sectors | 15.20 | 483x3.2 mm |
| Pb Converter | 12 Sectors | 15.50 | 432x1.0 mm |
| C Scint. | 12 Sectors | 15.80 | 457x3.2 mm |
| <u>Inner Wire Chamber (IWC)</u> | | | $L \simeq 74$ cm |
| Inner cathode | 384 strips | 26.47 | -45° S=3.06 mm |
| IWC anodes | 768 wires | 27.02 | Axial S=2.21 mm |
| Outer cathode | 384 strips | 27.57 | +45° S=3.19 mm |
| D.C. inner CF cylinder | | 30.20 | 0.75 mm |
| <u>D.C. Layer</u> | <u>Cells</u> | <u>Center</u> | <u>Halfwidth</u> |
| 1 | 56 | 34.70 | 1.947 cm |
| 2 | 64 | 40.80 | 2.003 cm |
| 3 (stereo) | 72 | 46.90 | 2.046 cm |
| 4 | 80 | 53.00 | 2.081 cm |
| D.C. outer CF cylinder | | 58.00 | 1.00 mm |
| D Scint. | 16 Sectors | 59.37 | 940x6.4 mm |
| Drift chamber 90.0 cm overall, active length $\simeq 85$ cm. Stereo angle is 7.0 deg. (layer 3), relative to axial. | | | |

corresponding one on the other plate were found to align within $\pm 50\mu\text{m}$.

The inner and outer carbon fiber (CF) cylinders hold the endplates together. These cylinders had thicknesses of 0.75 mm and 1.0 mm respectively. The inner surface of the outer CF cylinder was covered with a $75\mu\text{m}$ copper sheet and the outer surface of the inner CF cylinder with a $75\mu\text{m}$ aluminized mylar sheet. High voltage was applied to these conducting sheets to make the electric field, for the wires around them, more uniform. The outer carbon fiber cylinder was fastened after the stringing and replaced correctly the tension rods. This was clear after measuring

Table 3.2: Wires and tensions used

| Type of wire | Diameter (μm) | Material | Tension (grams) |
|-------------------|----------------------------|----------|-----------------|
| Anodes 1 and 10 | 150 | Aluminum | 220 |
| Anodes 2 and 9 | 25 | Tungsten | 70 |
| Anodes 3 to 8 | 20 | Tungsten | 50 |
| Cathodes 1 and 19 | 300 | Aluminum | 500 |
| Cathodes 2 to 17 | 150 | Aluminum | 200 |
| Cathode 18 | 178 | Aluminum | 260 |

the tensions in the wires with and without the outer carbon fiber cylinder.

Stringing The Drift Chamber consists of 272 cells, each cell having 19 cathodes and 10 anode wires. All 29 wires were gold plated. The wire numbering increases with increasing radial position, so that radial wire 1 in any layer is closest to the center of the detector. The cell geometry is shown in Figure 3.3. and wire details are given in Table 3.2.

The wires were strung with the chamber in the vertical position in the following manner: one operator on top would pass the wire through a pin, thread the wire in a magnetic needle, pass the needle through the hole in the feedthru and then lower the needle to meet a magnetized needle on the corresponding hole in the bottom. Once the wire was passed through the bottom hole the operator on top seated the pin in the hole and crimped the wire. The operator on the bottom passed the wire through a pin, seated the pin, hung the weight, and then crimped the wire. This could be done efficiently; a team of two could string 20 wires/hour. The chamber was tilted to string the stereo layer wires. The tensions were continuously monitored, and wires could be easily replaced before the chamber was finally sealed.

In order to measure the wire tensions a current was passed through the wire. By changing the frequency of this current in the presence of a magnetic field a

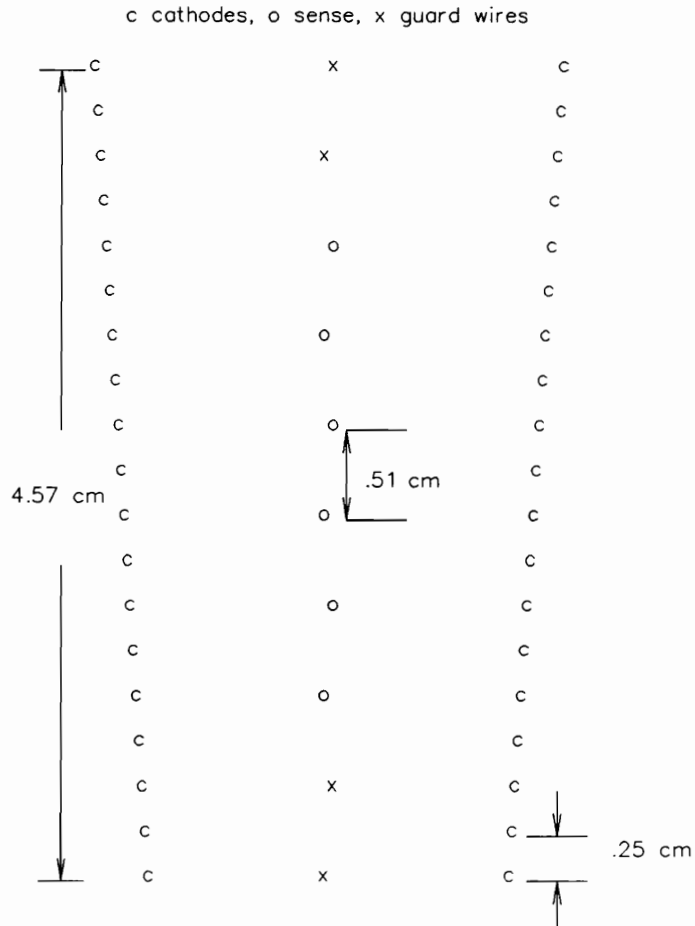


Figure 3.3: Cell geometry

resonance frequency was found. From the period of this resonance τ , the wire's length L and density ρ the tension, T , was deduced.

$$T = \frac{4L^2\rho}{\tau^2} \quad (3.1)$$

Due to the gold coating, total densities were computed assuming the manufacturers coating thicknesses. For further details see Henderson *et al.* [28].

Gas system The chamber has been operated with a gas mixture of 49.9%

argon and 49.9% ethane. Ethanol is added, 0.2%, by bubbling half of the argon through ethanol. This mixture gives for electric fields ~ 2.5 kV/cm, a drift velocity close to $50 \mu\text{m/ns}$. Around 90% of the gas is recycled and 10% is added from gas cylinders. Gas flow controllers regulate the total mixture to better than 1%. Filters in the recycling system remove mainly water and oxygen. The normal running flow is 2 liters/minute. The temperature and the pressure inside the chamber were monitored continuously by reading 8 thermocouples and 1 pressure transducer installed inside the chamber, located on the endplates.

High Voltage In order to apply high voltage to the cathodes, each layer of the drift chamber was segmented in three sectors. Six Bertan negative power supplies (model 375N) of two channels each, were needed to cover the 12 high voltage sectors. From the high voltage a lower voltage was also derived by using a resistor chain. The low and the high voltage were applied in parallel to the cathodes 1 and 19 respectively in a sector. Each cathode had 18 $2\text{M}\Omega$ resistors connecting the 19 wires. Since the cell sizes increase from layers 1 to 4, the high voltages needed to keep the electric field constant also increased in the same order. For typical operating voltages of 5.0 kV, 5.1 kV, 5.2 kV, and 5.3 kV applied to cathode wire number 19 of each cell for layers 1 to 4, the following potential drops between neighbor wires in one cell were obtained: 31.0 V, 33.6 V, 36.4 V, and 39.2 V. Where possible, all high voltage lines were carefully insulated with kapton to avoid breakdown. Also it was necessary to keep the chamber in a dry nitrogen atmosphere for operation at the desired voltages.

Since all parts of the detector share the same ground, namely the magnet's yoke, RC filters were installed in all the high voltage lines for the drift chamber. These filters ($R=10 \text{ k}\Omega$ and $C=.001 \mu\text{F}$, 10.0 kV) significantly reduced the noise

pickup, specially the 23 MHz from the radio frequency (RF) separator.

Electronics Of the 10 anode wires in each cell only the central 6 are read, for a total of 1632 readout channels. Preamplifier cards were mounted on the end plates by fitting the cards on the feedthru grooves. Coaxial ALPHA 9374 cables connected the preamp to the postamplifiers and ECL cables connected the postamplifiers to the LeCroy 1879 FASTBUS TDCs. The postamplifiers had a logic output for signals over threshold, and parallel analog outputs. No analog information was recorded in this experiment. Trigger cards were mated to the backplane connector of the TDCs which provides copies of the input signals. These cards provided a simple OR information for the 6 wires in the cell. If two or more wires were hit, the cell is registered as hit. These "OR boards" were interrogated by the SLAC Scanner Processor (SSP) for the pattern of the cells hit. The SSP decided whether to accept the event and write to the buffer or reject it and reset the electronics. A description of the trigger cards is found in Bennett *et al.* [29].

3.1.2 Performance

The following important parameters of the drift chamber were obtained:

Efficiency Two different methods were used to determine the efficiency of the chamber. In both cases cosmic ray events, with the magnetic field off, were used. In one method if a fit to a straight track is found, then a search was performed for those wires that should have but did not fire. In the other method no tracking is done, instead if the two neighbors of a wire fire the wire should also fire. Both methods are in agreement, the results are illustrated in Figure 3.4. The high voltages for the inner and outer carbon fiber cylinders were found to have little effect on the chamber efficiency and were set, as a mid value between ground and -5.0 kV, at -2.5

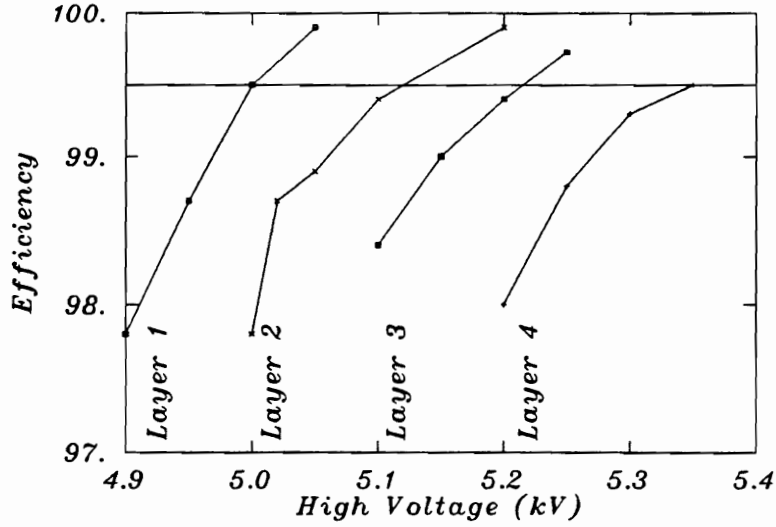


Figure 3.4: Drift chamber efficiency

kV each. The drift chamber efficiency was also measured, after the completion of this experiment, with the magnetic field on. However, because of the small Lorentz angle, the magnetic field had little effect on the efficiency and the chamber is still operated at the same voltages.

Resolution A resolution within the cell, ignoring tracking, as well as a resolution of the cell with respect to the rest of the chamber were determined. In the first method, two neighbors for each wire are assigned, the difference between the mean time of firing of its neighbors and the firing time for that wire is proportional to its resolution.

For wires $i=2,3,4,5$ the neighbors are $i+1$ and $i-1$. For these wires:

$$t = \frac{t_{i+1} + t_{i-1}}{2} - t_i \quad (3.2)$$

This distribution is centered at times corresponding to $\pm 2\delta$, where δ is the staggering. The resolution, σ , is found from:

$$\Delta = \sqrt{(\sigma/2)^2 + (\sigma/2)^2 + (\sigma)^2}, \quad (3.3)$$

then,

$$\sigma = \sqrt{2/3}\Delta. \quad (3.4)$$

For the sense wire 1 the neighbors are wires 2 and 4. For this case:

$$t = \frac{3t_2 - t_4}{2} - t_1 \quad (3.5)$$

$$\Delta = \sqrt{(3\sigma/2)^2 + (\sigma/2)^2 + (\sigma)^2} \quad (3.6)$$

$$\sigma = \sqrt{2/7}\Delta. \quad (3.7)$$

The neighbor wires for sense wire 6 are wires 5 and 3, and the resolution is determined as for wire 1.

In the above Δ is just the standard deviation of the distribution, and the coefficients (1/2, 1/2, -1) and (3/2, -1/2, -1) are just the partial derivatives of t , the statistical weight factors.

For wires 2 to 5, Δ is 2.8 nsec, or $140\mu\text{m}$ if the drift velocity is $50\mu\text{m}/\text{ns}$. This gives a resolution of $114\mu\text{m}$ for these wires. For wires 1 and 6 the resolution found in this method is $160\mu\text{m}$. The resolution of the fourth layer was consistently worse than the others, $130\mu\text{m}$ for wires 2 to 5. The intrinsic time resolution is 1nsec, or $50\mu\text{m}$. This is for the ideal case where all channels in the TDC's work as designed. TDC times are in 2 nsec buckets. Fractions ≥ 0.5 are passed as 1.0 and < 0.5 are passed as 0.0. Some channels however had a resolution of 2 nsec.

Figure 3.5 illustrates the benefits of staggering the anode wires. When a charged particle passes through the chamber, electrons drift towards the anodes. The TDCs record the time between the strobe and the avalanche produced in each wire. From these times a distance to the wire on both the left and the right side is reconstructed. As seen in Figure 3.5 the staggering enhances the differences for the

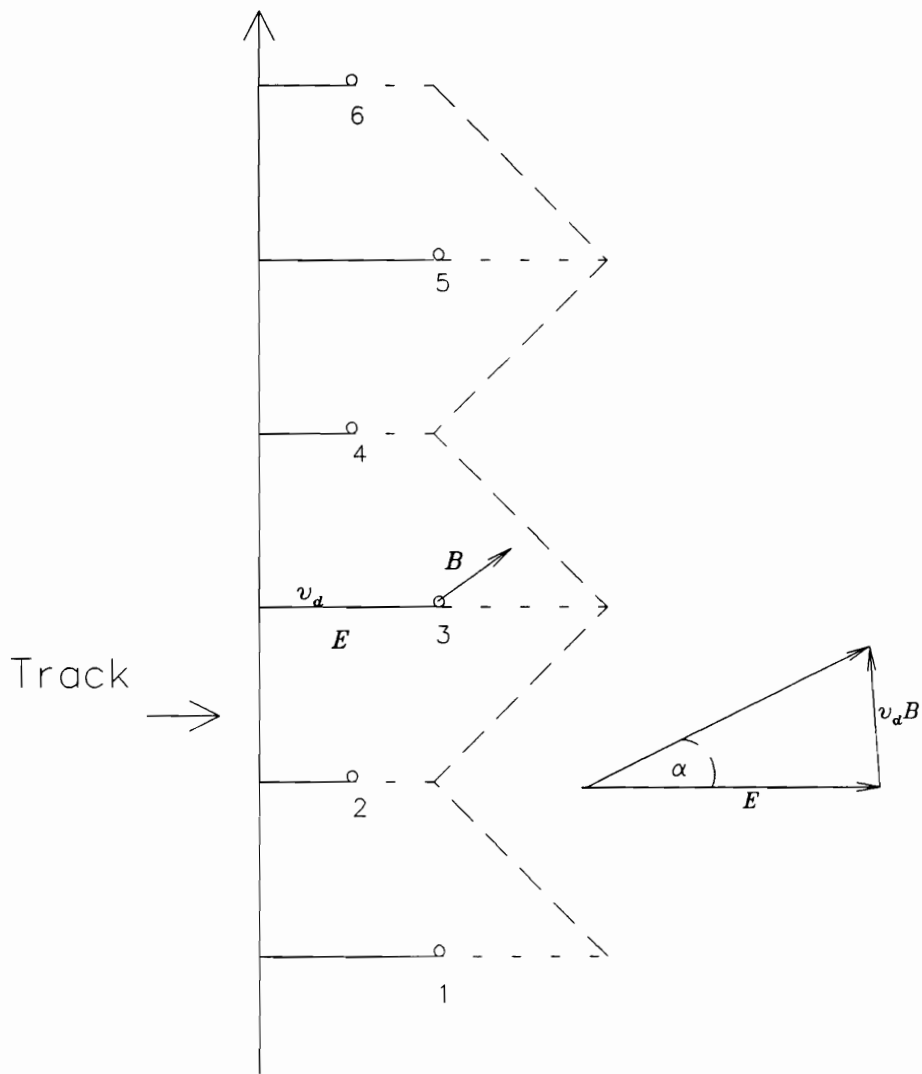


Figure 3.5: Staggering

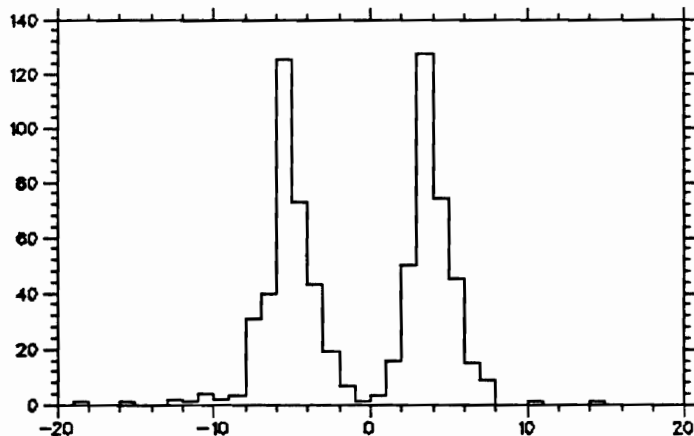


Figure 3.6: Drift times (2nsec buckets)

points on the wrong side of the actual drift. A fit to a straight line should resolve the left right-ambiguity.

A better way of determining the resolution is by fitting tracks to the points reconstructed from the TDC times. In this method the resolution is taken to be the track residuals, i.e., the differences between the reconstructed points and the parametrized track point. The track points are found by a least squares fit to the experimental points. The standard deviation of the sum of all the residuals represents the average position resolution for the whole chamber. Best fits for optimized physical detector parameters, gave an overall resolution of $\sigma_T = 270\mu\text{m}$. But taking the intrinsic TDC resolution of 1 nsec and adding a 1nsec uncertainty in determining the TDC leading edge time, we obtain a 1.41 nsec time resolution, or $71\mu\text{m}$.

In principle one should be able to improve the overall $270\mu\text{m}$ first found. Due to the uncertainties in the wire positions, a first correction to the wire positions was tried. If the assumed position for a wire is shifted with respect to its actual position, then the residuals should decrease when appropriate shifts are added to

the assumed wire positions. After using these corrections to the wire positions, a new set of pedestals (see below) has to be calculated. After a few iterations, the time and position corrections became negligible, and the overall resolution improved to $245\mu\text{m}$. Smaller corrections were introduced, like to account for the Z position of the avalanche in a wire. The best resolution at this point is $240\mu\text{m}$. The overall resolution is still enough to resolve the left right ambiguity, since: $\delta=250\mu\text{m}$, the distance between the peaks of Figure 3.6 is $4\delta=1000\mu\text{m}\gg 240\mu\text{m}$.

Pedestals : From the total TDC time, the actual drift time needs to be recovered since the distance from the track to the wire is $x=v_d \times t_d$, or $x=v_d \times (\text{TDC}-\text{PEDESTAL})$, where v_d is the drift velocity. Because of this linear relation between distance and pedestal it is crucial to determine the pedestals to high accuracy if high resolution is to be achieved. The TDC time in the limit where the drift time goes to zero is the pedestal. This pedestal includes: internal TDC delay, time from the avalanche to the input of the TDC, trigger decision time depending on the C counter that fired, etc. The pedestals were determined from straight tracks for muon decay electrons with the magnetic field set to zero. The time distributions were fitted to an error function. The pedestal is the time for which the height of the function is half the full height. Since this distribution is quite steep this method required huge statistics, and satisfactory pedestals were calculated for each of the 1632 sense wires of the chamber with an accuracy of 1nsec ($50\mu\text{m}$). Although the pedestals proved to be stable, they were monitored regularly, and appropriate pedestal files were produced for each run.

Drift velocity : By minimizing the residuals in the track fitting, drift velocities were found for all 24 radial positions. In this method the residuals are calculated by trying different values for the drift velocity. The drift velocity that

minimizes the residuals is taken to be the correct one. Another method is to fit to a gaussian one side of the distribution in Figure 3.6. The mean of the gaussian fit is the drift time for a distance equal to twice the staggering. Using the design value for the staggering, $253\mu\text{m}$, the drift velocity is the ratio between staggering and drift time. Because these times are short, $\sim 10\text{nsec}$, the accuracy of this method is correlated to the intrinsic resolution of the TDC. The values obtained this way $49.4\mu\text{m/nsec}$ were typically 4% lower than the ones found by the residuals $51.4\mu\text{m/nsec}$, but had an accuracy of the order of 5%. The drift velocities found were $\sim 5\%$ higher than those deduced from the tables for the gas mixture used. Very small, variations $< 1.0\%$, were seen for the 24 radial positions. The drift velocity was obtained with the magnetic field on.

Lorentz Angle : Because of the magnetic field, the drift towards the anodes deviates from the electric field lines. This deviation is proportional to $v_d \times B$. See Figure 3.5. The Lorentz angle α is given by: $\tan\theta \sim v_d \times (B/E)$. At 2.7 kG, $E \sim 2.6\text{ kV/cm}$, and $v_d = 50\mu\text{m/ns}$, the Lorentz angle should be $\sim 5.2^\circ$. By a minimum χ^2 search in the track fitting, a higher value was found: $\alpha \sim 6.2^\circ \pm 0.5^\circ$. When running at different magnetic fields the Lorentz angle α was scaled with respect to the 2.7 kG value.

3.2 Inner Wire Chamber

To reconstruct the Z coordinate of a track the third layer of the drift chamber was wired in stereo, providing one axial track coordinate. Additionally a cylindrical proportional wire chamber (IWC) was placed just inside the inner radius of the drift chamber. This 0.5 cm. cylindrical chamber consists of an inner layer of 384 cathode wires, 768 anode wires, and 384 outer cathode wires. A projection of these

3 wire layers, for a typical event, is illustrated in Figure 3.7.

The axial and angular position of a track are given by the wire crossings of the hit anode wires and the cluster centroid from at least one of the cathode planes, as shown in Figure 3.8. The radial position is the anode's radial distance. The electronics readout is performed by a system of RMH preamplifiers, receivers and encoders. This chamber was borrowed from the ASTERIX collaboration (C2), and the same readout system as described by Ahmad *et al.* [30] was used. Construction details can be found in Bird *et al.* [31]. The position resolution was 1.0 mm. The chamber is operated with a gas mixture of 77.6% argon, 22.2% isobutane and 0.2% freon bubbled through methylal. An efficiency of $\sim 98\%$ was obtained for an operating voltage of 3.4 kV for the anodes and ground for the cathodes.

3.3 The Magnet

A large volume solenoid magnet was used to produce an axial magnetic field. The whole detector is fitted in the volume inside the magnet: 152 cm horizontally, 122 cm vertically and 117 cm axially or beam direction. A full survey of the magnetic field inside the magnet was conducted by using 12 Hall probes and one NMR fixed probe. The Hall probes were placed on an arm spaced every 5.0 cm and covering the radial region from 0.0 to 50.0 cm. The Hall probes were rotated and read for 0.0 to 345° in 15° steps. The whole process was repeated by reading the probes from -50.0 cm to +50.0 cm in the axial direction, in 5.0 cm steps. The central, main, coils and the end coils were powered independently. A ratio of 0.8 between main and end coil currents gave the most uniform magnetic field configuration. All the data was taken at 2.74 kG and the magnetic field was found to be uniform within $\pm 0.5\%$. For data taking only one NMR probe close to the upstream magnet

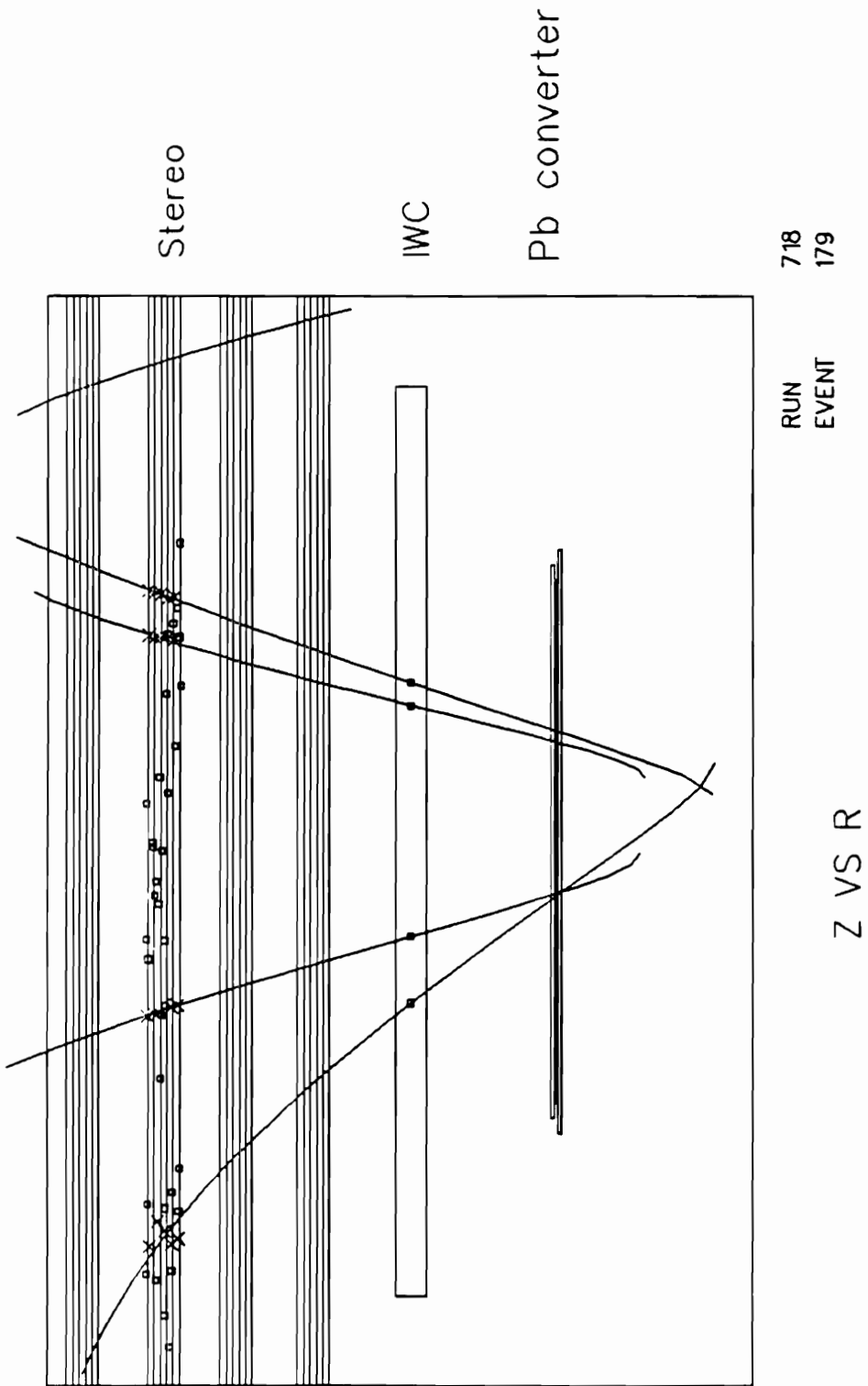


Figure 3.7: ZR view of an event

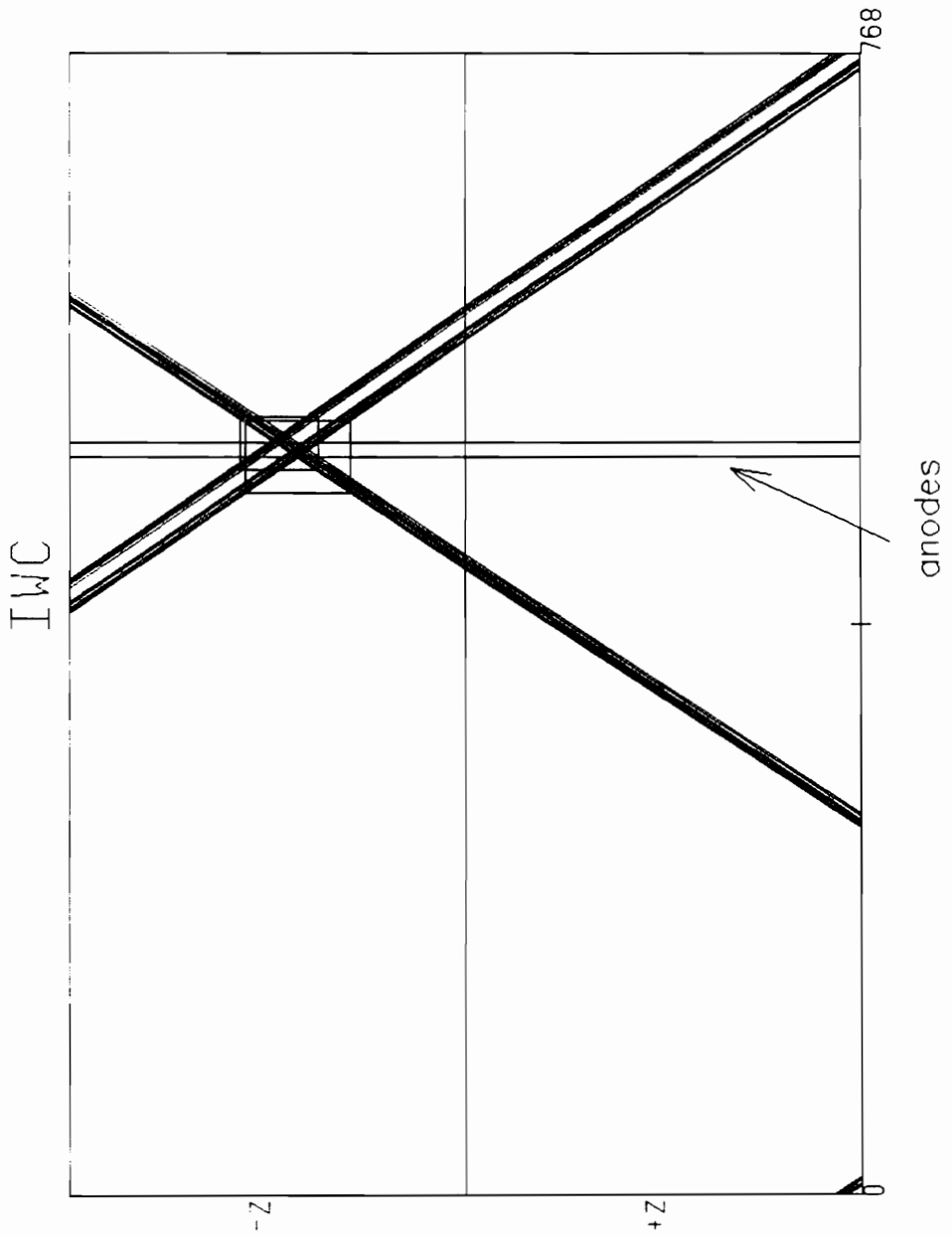


Figure 3.8: Wire crossings in the IWC

Table 3.3: Dimensions of the targets used. All targets were mounted perpendicular to the beam axis.

| Target | Shape | Dimensions | Foils | Spacing |
|--------|-------------|----------------------------------|-------|---------|
| Pb | rectangular | 15.0 cm × 13.5 cm × 0.020 cm | 10 | 0.94 cm |
| Sn | square | 12.5 cm × 12.5 cm × 0.033 cm | 11 | 1.0 cm |
| Mo | square | 12.5 cm × 12.5 cm × 0.025 cm | 7 | 1.1 cm |
| Ca | square | 10.2 cm × 10.2 cm × 1.96 cm | 1 | |
| Al | disc | 15.0 cm diameter × 1.92 cm thick | 1 | |
| Si | disc | 8.4 cm diameter × 2.00 cm thick | 1 | |

wall was monitored. From the value given by this probe, and by using the magnet survey data, the magnetic field inside the drift chamber was found. The downstream magnet wall had a 25.4 cm diameter hole that allowed access to change the targets.

3.4 Targets

The physical dimensions of the six different targets were dictated by optimizing the muon stops, minimizing the photoconversion in the target and having roughly the same attenuation length (thickness X density). The tin, molybdenum, and lead targets were made of several foils spaced along the beam direction. The aluminium and calcium targets were solid pieces and the silicon target was granulated and enclosed in a thin cylindrical plastic container. All the target dimensions are specified in Table 3.3.

3.5 Beamline

The detector was located at the end of the M9A leg of the TRIUMF's cyclotron. A 500 MeV proton beam, 130 μ A current, hits a 10 cm long beryllium target. A fraction of these protons will produce pions, and by taking pions at 135° with the incoming proton beam, a small fraction of the pions produced are directed along

the M9A beamline. From pion decay, muons arrive at the detector at a rate of 4×10^5 /sec. Since a large number of pions undergo radiative capture in these targets, a radio frequency separator (RFS) was installed, 9.5 m upstream of the targets, to reduce the number of pions that make it to the target. The RFS uses a RF voltage and a horizontal DC magnetic field. The principle of the RFS operation is the following: the muons ($\beta \sim 0.6$) arrive at the RFS approximately one-half an RF period before the pions ($\beta \sim 0.5$) from the same proton pulse, and the electrons from the following proton pulse. The phase of the RFS is then adjusted so that the peak of the RF voltage coincides with the muon time of arrival. Ideally pions and electrons arrive when the electric field is reversed and the electric and magnetic forces work in the same direction to deflect these particles. By using the RFS, the π/μ ratio was reduced at the target by a factor of 10^3 . Offline time cuts were used to further eliminate pion induced events. For a full description of the RFS used in the experiment, and a layout of the M9A beamline, see Blackmore *et al.* [32].

3.6 Cosmic Counters

Plane wire chambers (12) and scintillators (23) were used to help eliminate, during data analysis, cosmic induced events. These chambers and scintillators covered the top of the magnet's yoke and around one third of the upper part of the magnet's walls. The total data for any of the targets was collected in almost one day of running. For these high rate situations, the cosmic induced events represented a negligible contribution to the data.

3.7 Trigger Scintillators

Scintillators were used for the initial triggering as well as for vetoing and counting muon stops. In front of the magnet 4 scintillators, with two phototubes each, were placed. The signals from the two tubes were combined. A muon stop was defined as all 4 beam counters firing and in coincidence with a muon arriving at the target as determined by the RFS phase. Four scintillators (A), arc shaped, enclosed the target region. In addition four more scintillators (A'), of same arc shape, covered the first four and eliminated gaps. These eight scintillators were used in the triggering, for vetoing charged particles leaving from the target. A polygonal tube of 12, flat, scintillators (B) were placed just inside the lead converter. And 12 scintillators (C) covered the 1.08 mm lead converter. If a pair was created in the lead by a gamma, then the condition $\overline{B} \cdot C$ had to be satisfied. A set of 16 panels of flat scintillators (D) covering the outside of the drift chamber, were used to select those pairs for which both particles came out of the drift chamber, and did not wrap around. The D scintillators were covered with a sandwich of 3 mm of aluminum, 4 mm of lead and 3 mm of aluminum. These layers were used to avoid re entry of any of the particles in the pair into the drift chamber. The trigger condition required at least 2D counters to have fired. Finally, a veto counter (V) was placed behind the targets to make sure that the muon which arrived in time with the RFS, had indeed stopped.

Chapter 4

Data Analysis

4.1 Introduction

The main four aspects of the data analysis to be discussed are the following:

- **Track Reconstruction:** the energy of each pair particle is reconstructed from the raw information passed by the RMC detector. To ensure that the photon reconstructed actually corresponds to a valid RMC event, some software cuts are applied to the data. The track reconstruction as well as the cuts used are described in section 2.
- **Monte Carlo:** in order to use the reconstructed energy spectrum, one needs to understand how the detector behaves, i.e. the response function. One simulates all the physical processes and detector components and compares with real data for some measured process. A discussion of the response function as well as the acceptance is presented in section 3.
- **Corrections:** because of inefficiencies, backgrounds, etc. one needs to make corrections to the data and determine the experimental errors. This is described in section 4
- **Branching ratios:** the final goal of the analysis is to produce the different RMC/OMC branching ratios for all six targets. All the aspects of the analysis mentioned above are used to produce these ratios.

4.2 Track Reconstruction

The energy of a photon is the sum of the electron and positron energies. The energy of any of these pair particles is :

$$E = \sqrt{P^2 + m^2} \quad (4.1)$$

where

$$P = \sqrt{P_{\perp}^2 + P_{\parallel}^2} \quad (4.2)$$

and m is the particle's rest mass. The trajectory of either of the pair particles in a constant magnetic field \vec{B} is a helix. The momentum component perpendicular to \vec{B} is proportional to the radius of curvature R ,

$$P_{\perp} = 0.3BR \quad (4.3)$$

where B is in kilo gauss, R in cm and P in MeV/c. The radius of curvature is found from the XY fit given by layers 1,2 and 4 of the drift chamber. To calculate the axial momentum one needs to know the pitch angle which is found from the Z fit of the track by using the IWC and the DC stereo layer,

$$P_{\parallel} = 0.3BZ_{circ} \quad (4.4)$$

where $Z_{circ} = R \tan\lambda$, and λ is the pitch angle.

4.2.1 Transverse momentum

To find the transverse momentum, one needs to reconstruct the radius of curvature for the track. The wire positions were first assumed to be the designed ones. Then, left-right asymmetries of the track-to-wire distances were examined to determine corrections to these wire positions, and a new wire position map of the DC

was created. To reconstruct a track in the DC one adds to the wire's position, the distance travelled by the charge avalanche. These drift distances are reconstructed from the drift times as passed by the TDC's, (after pedestal correction) and the drift velocity. In a first iteration it is assumed that the avalanche travels along the straight electric field lines, perpendicular to the sense wire's plane as shown in Figure 4.1. A fit to a circle is tried for each track using these points. However, the early avalanche for a non-radial track may well be along a different field line, as shown in Figure 4.1, and then a correction to the track points is applied. Assuming that the contour of constant drift times is a parabola, this correction can be shown to be

$$C = (W/8)\tan^2\theta \quad (4.5)$$

where θ is the track inclination angle and W is the spacing between sense wires, see Wright *et al.* [33]. From the track points that give the best fit, that is the smallest residuals or difference between reconstructed points and points on the fitted curve, the radius of curvature for each track is obtained. Ideally 18 points will be used. To avoid biasing the fit by a few bad points, if the chi-squared of one point is greater than 4 times the average chi-squared of the track, then that point is dropped and a new fit is tried. Once the radius of curvature is known, then its projection in the axial direction is attempted.

4.2.2 Longitudinal momentum

The longitudinal momentum is reconstructed from the Z projection of the particle's trajectory. From the IWC one obtains a first Z point and from the DC stereo layer, 6 more Z points are produced. The radial position of each point is the radial position of the detector's element, the DC stereo wire or the IWC. Because

of the constant velocity of the particles, there is a linear relationship between the Z-coordinate and the rotation angle in the XY plane, i.e. the track is a helix. The slope in this projection is $\tan\lambda$. The Z momentum cannot be reconstructed without knowing the radius of curvature, and a good XY fit is required before the Z fit is done.

4.2.3 Software Cuts

Two different types of cuts are applied to the data to ensure: first a good track reconstruction, and second that the photon that produced the pair actually comes from the target. There are two levels of the track reconstruction cuts: In the first level are the cuts one imposes when reconstructing the radius of curvature for any particle. They include: maximum chi-squared of the fit, minimum number of points etc. The second level of cuts are applied to the tracks already reconstructed to ensure a good pair coming from the target region. These cuts are listed in Table 4.1 as used in version 2.2 of the RMCOFIA analysis by the RMC group at TRIUMF.

The efficiency of these cuts in eliminating bad fits is tested by running with a μ^+ beam. By momentum conservation, the maximum energy of any of the decay particles is half the muon mass $\approx 53\text{MeV}$. Then, if the positron radiates by bremsstrahlung, the maximum energy of the photon produced should not exceed 53 MeV. The histogram shown in Figure 4.2 illustrates that the contamination in the $E > 57\text{ MeV}$ region, due to poorly reconstructed events, is negligible.

In addition to these cuts, a cut to reject cosmic-ray induced events was used. Most of the pairs seen in a cosmic ray run are single muons reconstructed as two particles coming from the center of the target. All these events are cut due to large opening angle, large distance between tracks at the converter etc. However

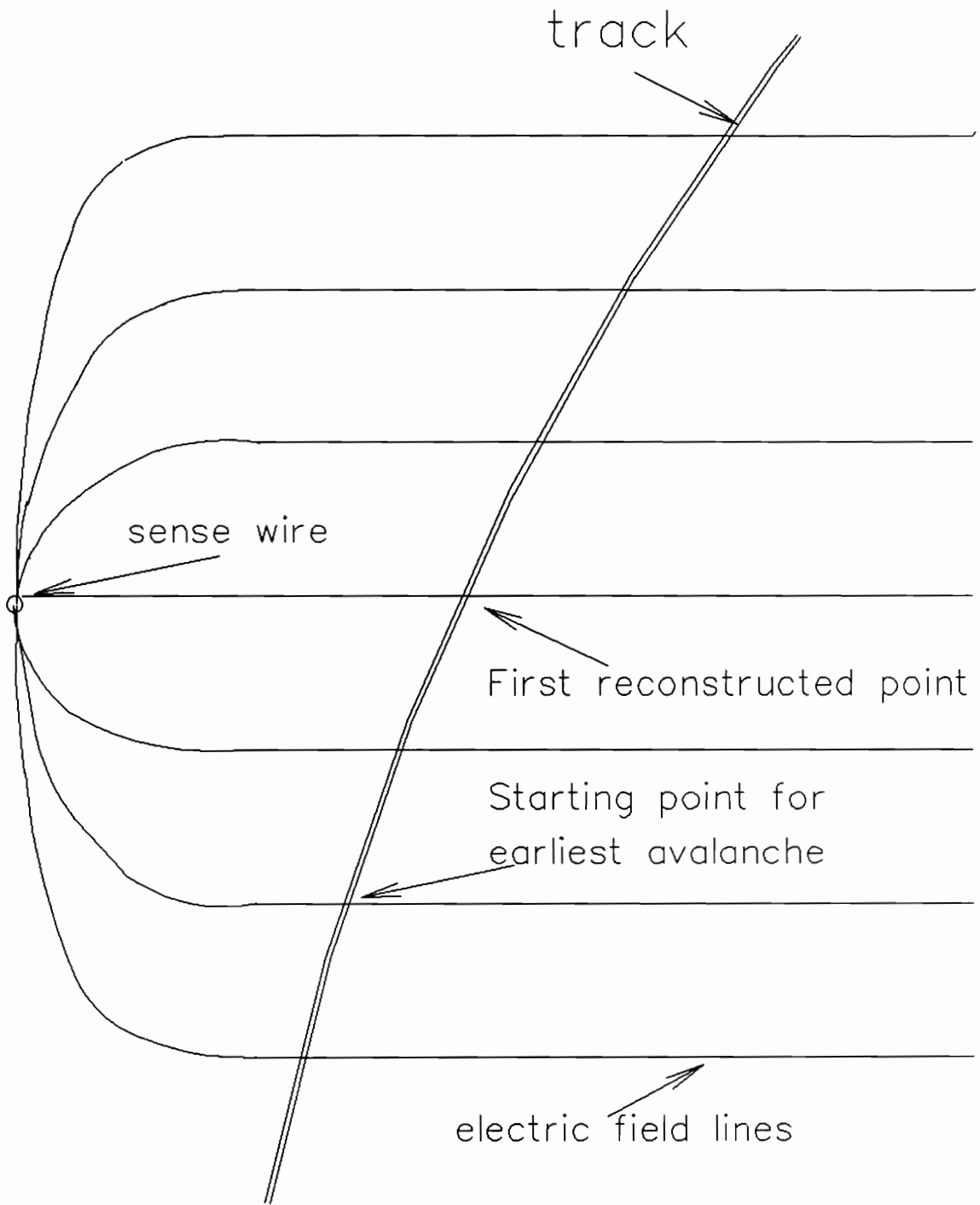


Figure 4.1: Drift distance for curved tracks

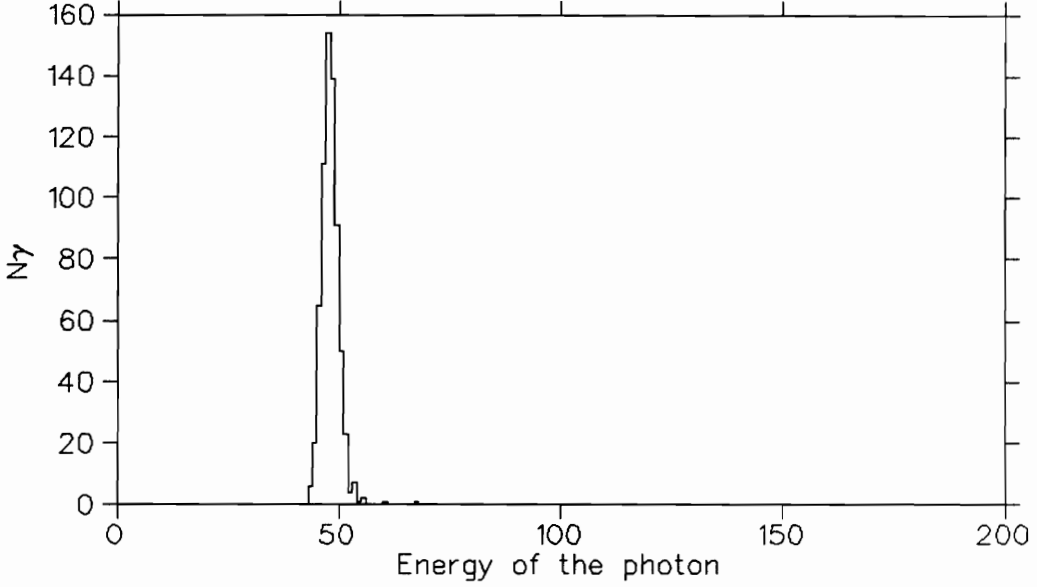


Figure 4.2: High energy tail as measured with μ^+ stopped in liquid hydrogen

some real photons in the detector are produced by cosmic rays. Most of these photon events were rejected if the number of D counters plus the number of prompt cosmic-ray chambers plus the number of prompt cosmic-ray scintillators, was > 5 . By running the detector with cosmic rays, using the same trigger that was used in data taking, and applying the same cuts that were used for the data analysis, the number of cosmic-ray induced events per day with $E_\gamma \geq 57$ MeV was 2.3 ± 0.4 . All the data for any nuclear target was collected in less than one day, and the cosmic ray background was $< 0.4\%$.

Finally, if the photon detected does come from capture in the target, it should be delayed with respect to the arrival of the muon. Because the pion radiative capture process is several orders of magnitude larger than the signal from RMC ($\sim 10^{-2}$ as compared to $\sim 10^{-5}$) then any small pion contamination causes a photon background larger than the RMC signal. To cut these events the following

Table 4.1: Cuts to the reconstructed pairs

| Description | Value |
|---|----------|
| Distance between tracks at the converter in X and Y | 4.5 cm |
| Distance between tracks at the converter, in Z | 10.0 cm |
| Opening angle | 50.0° |
| Maximum Z at R= 8.0 cm, downstream | 11.0 cm |
| Minimum Z at R= 8.0 cm, upstream | -18.0 cm |
| Maximum Z of closest approach, upstream | 10.0 cm |
| Minimum Z of closest approach, downstream | -12.0 cm |
| Minimum number of points in e^+ track | 14 |
| Minimum number of points in e^- track | 11 |
| Maximum χ_{xy}^2 of e^+ track | 0.01 |
| Maximum χ_{xy}^2 of e^- track | 0.012 |
| Maximum χ_z^2 of e^+ track | 0.15 |
| Maximum χ_z^2 of e^- track | 0.15 |
| Maximum ratio P_z/P_{tot} | 0.8 |
| Minimum number of points in 4 th layer | 3 |
| Maximum difference between IWC and projected angle | 1.0° |

was used: First, pions lose more energy when passing through the beam counter scintillators; this means a larger beam counter pulse height as compared to muons. Second, the outgoing gamma following pion capture is in time with the pion arrival (delayed $\sim 10^{-10}$ sec). And third, the pions should arrive out of phase with respect to the muons, because of separation at the RFS as described in Chapter 3. To demonstrate elimination of these pion-induced events, also called prompt events, data for pion capture in all six targets was collected. The prompt cut rejected events under any of the following conditions:

- Any beam counter ADC over threshold and there was no recent muon according to the RFS phase.
- Any beam counter CAMAC TDC was "prompt", and either there was no recent muon or there was a recent muon but at least two beam ADC's were

over threshold.

- Any beam counter ADC above a very high value, typical of pions stopping in a beam counter.

Since the event time is given by the C counters, and the walk times for all 12 counters are different, the CAMAC TDC's were corrected according to the C counter that fired. In addition a smaller time correction was used to account for the travelling time of the light pulse in the scintillators.

To estimate the efficiency of these cuts one first measures the pion contamination in the RMC spectrum by counting the number of events with $E_\gamma > 100$ MeV. Figure 4.3 illustrates the large pion contamination in the RMC spectrum for lead, and the efficiency of the prompt cut by removing nearly all the events with energies above 100 MeV. Since all the remaining events above 100 MeV should come from pion capture, one estimates from the radiative pion capture spectrum, the corresponding fraction of events below 100 MeV. The remaining pion contaminations for all six targets were less than 0.7 %.

However some RMC events may occur near the prompt time and one needs to know what fraction of the RMC events have been falsely rejected as prompt. This was done by comparing the spectrum of the events rejected as prompt with the sum of the radiative pion capture spectrum and the RMC spectrum for the target in question. Figure 4.4 shows the energy spectrum for events rejected as prompt in RMC in lead, and the radiative pion capture spectrum in that target. The fraction of RMC events that has to be added to a normalized radiative pion capture spectrum to obtain the prompt spectrum, represents the fraction of good RMC events rejected as prompt. The percentages of good RMC events rejected by the prompt

Table 4.2: Effect of prompt cuts

| Target | RMC events rejected (%) |
|------------|-------------------------|
| Lead | 1.6 ± 1.1 |
| Tin | 1.4 ± 0.7 |
| Molybdenum | 0.6 ± 0.4 |
| Calcium | 1.9 ± 0.5 |
| Silicon | 2.1 ± 0.5 |
| Aluminum | 0.0 ± 0.4 |

cut for all targets are listed in Table 4.2.

4.3 Monte Carlo

Several different, well known processes, were studied in order to calibrate the detector. One was radiative pion capture and pion charge exchange on hydrogen and the other was radiative pion capture in carbon.

$$\pi^- p \rightarrow \gamma n \quad (60.4\%) \quad (4.6)$$

$$\pi^- p \rightarrow \pi^0 n \rightarrow \gamma \gamma n \quad (39.6\%) \quad (4.7)$$

$$\pi^- C \rightarrow X \gamma \quad (4.8)$$

The π^0 decays into two photons (98.8%) in 8.4×10^{-17} sec. In GEANT a photon spectrum is generated, in the target region of the detector, with the appropriate energy distribution. All the possible physical processes through which these photons can interact are implemented in the GEANT Monte Carlo simulation. The fraction of those photons that convert and produce a valid trigger are then analyzed with the track reconstruction program used for real data. The response function must mimic the effect of analysing those events as seen by the detector. To find the response function of the detector, one uses the input spectrum and applies to it the

mathematical operations that represent the detector behavior. What this means is, given N photons of energy E , the response function will take the fraction that is seen by the detector and will distribute them across the energy spectrum according to the resolution and energy loss in the detector. When comparing a measured energy spectrum with a theoretical one, the theoretical spectrum is passed through the response function and the result is compared to the observed one.

In principle one would like to reconstruct from the observed spectrum, the input that produced it. However this inverse problem is analytically hard to solve. Basically what this means is that it is easier to mimic the functions that distribute the counts across the energy spectrum than to find the function that collects them and puts them back in their original bins. The analytical requirement is obtaining the inverse of a large matrix. Because experimental spectra are not smooth and because there are very few counts in some bins, the errors in the inverse matrix are so large that this solution is not practical.

To find the response function, monoenergetic photons were generated using the GEANT simulation for the detector, at 10 MeV intervals between 50 and 140 MeV. The output was analyzed as real data, and the reconstructed photon energy spectra were fitted to a response function of the form:

$$D(E_\gamma, E) = A \exp \left[-\frac{1}{2\sigma_0^2}(E - E_0)^2 \right] + F \exp \left[-\frac{1}{2\sigma_3^2}(E - E_3)^2 \right] \quad \text{for } E_1 < E < E_2 \quad (4.9)$$

$$D(E_\gamma, E) = B \exp \left[-\frac{1}{2\sigma_1}(E_1 - E) \right] + F \exp \left[-\frac{1}{2\sigma_3^2}(E - E_3)^2 \right] \quad \text{for } E < E_1 \quad (4.10)$$

$$D(E_\gamma, E) = C \exp \left[-\frac{1}{2\sigma_2}(E - E_2) \right] + F \exp \left[-\frac{1}{2\sigma_3^2}(E - E_3)^2 \right] \quad \text{for } E > E_2 \quad (4.11)$$

where

$$E_1 = E_0 - \frac{\sigma_0^2}{\sigma_1} \quad (4.12)$$

$$E_2 = E_0 + \frac{\sigma_0^2}{\sigma_2} \quad (4.13)$$

and

$$B = A \exp \left[-\frac{\sigma_0^2}{2\sigma_1^2} \right] \quad (4.14)$$

$$C = A \exp \left[-\frac{\sigma_0^2}{2\sigma_2^2} \right] \quad (4.15)$$

and A , F , E_0 , E_3 , σ_0 , σ_1 , σ_2 , and σ_3 are free parameters. E_γ is the actual photon energy and E is the reconstructed energy. In the energy range of interest this chosen function was found to represent the Monte Carlo prediction results quite well. The parameters E_0 , F , σ_0 , σ_1 , σ_2 and σ_3 were then fitted to polynomial functions of E_γ , e.g.

$$\sigma_0 = P_0 + P_1 E_\gamma + P_2 E_\gamma^2 + P_3 E_\gamma^3 \quad (4.16)$$

With this parameterization of the detector one could take any input, theoretical spectrum and obtain the output of the detector without having to run lengthy Monte Carlo simulations. Figure 4.12 shows an input spectrum and the same spectrum after its convolution with the detector response function.

One of the most important detector characteristics is the acceptance. What fraction of the photons generated in the target in some energy window will be detected and reconstructed in that same energy region? The main factors involved in the acceptance are the following: First, the solid angle. The detector is cylindrical open in front of the target to accept the beam, and at the back to allow target handling and operation. The solid angle of the detector is 79% of 4π . Second,

the probability of the photon to convert in the lead. A thin lead converter was chosen so that only $\sim 8\%$ of 80 MeV photons will convert. The photoconversion probability is energy dependent as shown in Figure 4.5. The photoconversion can happen anywhere in the lead and the pair particles multiple scatter as they pass through the converter. A larger acceptance could have been obtained by using a thicker converter, however because of multiple scattering in the converter the energy resolution would have been worse. Third, to have a 2D trigger as required in this experiment both particles have to fire the D scintillators. Low energy particles wrap around due to the magnetic field and a good fraction of the events are lost because one of the pair particles does not reach the D scintillators. One could either lower the magnetic field to increase the acceptance or change the trigger condition to require only that one of the pair particles reaches the outside. This implies a much higher event rate which the data acquisition system could not handle at the time of this experiment. A lower field also means poorer resolution and so a larger high energy tail background. However, for the RMC in protium experiment running now with the same detector, a 1D trigger and 2.4 kG field were shown to be practical. Finally, the acceptance also includes the ability to reconstruct a track in the DC.

The efficiency of the trigger as a function of the photon energy is shown in Figure 4.6.

Another important detector parameter is the energy resolution. This is best illustrated in the photon spectrum from radiative pion capture (see equation 4.6). From simple kinematics for this two body process, the energy should be 129.4 MeV. The measured resolution at this energy agrees with the Monte Carlo simulation as shown in Figure 4.7. One can also generate photons of any energy, and compare the Monte Carlo results with those given by the response function. This is shown

in Figure 4.8.

The radiative pion capture in ^{12}C process was chosen to test the GEANT response function. Using as input the data of Perroud *et al.* [34] passing this through the detector's response function and comparing to the measured one, the agreement seen is excellent. See Figure 4.9.

Better agreement was obtained in this case than with the charge exchange reactions in hydrogen. This is the main reason for using carbon as the calibration run.

4.4 Corrections, backgrounds

To determine the branching ratios one needs to know and understand well first the number of muons that were captured, second the number of photons seen with $E \geq 57$ MeV and third the detector's acceptance in this energy region.

4.4.1 Counting the captured muons

The number of muons captured in the target is equal to the number of muons that stop multiplied by the fraction that capture in that target.

The stops were counted by the 4 plastic scintillators in front of the target and a veto counter behind them. The scaler that counted the stops corresponded to the logic signal defined as all 4 beam counters firing, in coincidence with a muon time of flight with respect to the cyclotron RF. The plastic scintillators had a decay constant of ~ 3 nsec, which means that the odds of missing a muon at a rate of 400000/sec, with the typical cyclotron frequency of 23 MHz, are almost null. The combined inefficiency of the counters was $\leq 1\%$. However the A counters, that

surround the target, were part of the master veto and were erroneously set at a high voltage, well above the plateau value. This caused vetoing of some good muon stops. To correct for this mistake the random events accepted by the data acquisition were analyzed. Random events are accepted by opening a random gate, during data acquisition, and recording all values for the detector components. No trigger condition is imposed, but the ratios between the muon seen by the beam counters and those hitting the veto, as well as any other scintillator counter, should remain the same for any given target. From the pulse heights in the beam counter scintillators and the time with respect to the cyclotron RF one counts the muons arriving. If for that muon arrival, the veto counter or any of the A, A', and B counters do not present a pulse height typical of a muon passing through those scintillators, then the muon is counted as a good stop. From this analysis appropriate corrections for the muon stops were derived.

The fraction of the muon stops that capture is derived from the total disappearance rate for each target. From the bound μ^- life time and the μ^+ life time the capture fractions are calculated as;

$$\Lambda_t = \Lambda_c + Q\Lambda_d \quad (4.17)$$

where, $\Lambda_t = 1/\tau_{\mu^-}$, $\Lambda_d = 1/\tau_{\mu^+}$ and Q is the Huff factor that accounts for the fact that the normal muon decay rate is reduced because the binding of the muon reduces the energy available in the decay. The lifetimes and Huff factors were taken from Suzuki *et al.* [35], and are listed in Table 4.3. Lifetimes were also calculated in this experiment and are listed in parentheses in Table 4.3. However, because of our time window (800 ns) only short lifetimes, for heavy nuclei, could be fitted successfully. Figure 4.11 illustrates the time distribution of the photons following a muon stop for lead and tin. By fitting this time distribution to an exponential

Table 4.3: Lifetimes and Huff factors used to calculate the muon capture fractions

| Element | Mean life (ns) | Huff factor | Capture fraction |
|---------|------------------------------------|-------------|------------------|
| Al | 864.0 ± 1.0 (-) | 0.993 | 0.608 |
| Si | 756.0 ± 1.0 (-) | 0.992 | 0.657 |
| Ca | 332.7 ± 1.5 (290 ± 50.0) | 0.985 | 0.849 |
| Mo | 99.6 ± 1.5 (104 ± 5.0) | 0.936 | 0.955 |
| Sn | 92.1 ± 1.5 (92.6 ± 5.0) | 0.918 | 0.958 |
| Pb | 75.4 ± 1.0 (74.5 ± 5.0) | 0.844 | 0.966 |

decay plus a constant background, one finds the lifetime of the muons when bound to the nuclei of that target. Although a fit can be found for Al and Si, as can be seen in Figure 4.10, the large errors make these values worthless.

4.4.2 Counting photons

Besides the contaminations mentioned above, from pions, cosmic rays and external bremsstrahlung, the following corrections to the number of gammas were needed:

- Target absorption: The RMC photons produced in the target can interact with the target before leaving it either by creating a pair or by knocking off an electron (Compton scattering). In either case those events will be vetoed by the data acquisition as charged particles. To estimate the target effects, a large number of photons were generated in GEANT for a vacuum target and for all the six targets used. After analysis of these Monte Carlo events, the ratio between the target and the vacuum acceptance was taken as the corresponding target correction. A typical RMC spectrum shape was assumed for

the input spectrum for all the targets.

- **Stops in carbon:** A small fraction of the muons stop in carbon (in scintillators) giving rise to photons, with the typical RMC energy, but not coming from the right target. This fraction was estimated by analyzing good photon events with a large pulse height in the scintillators.
- **Bremsstrahlung:** Besides the radiation from muon decay particles (external bremsstrahlung) the muon itself can also radiate (internal bremsstrahlung). Bound muons can emit photons with an energy above 53 MeV depending on the relative velocity of the muon to the emitted photon (Doppler effect). This spectrum has been calculated by Hanggi *et al.* [36], and a simple extrapolation for the targets used shows a negligible contribution over 57 MeV. Also, due to our low acceptance for gammas under 50 MeV very few of these bremsstrahlung photons are seen even below this energy.
- **Veto scintillators:** the event is vetoed if any of the scintillators in the three rings that surround the target fire. Because the A and A' counters were operated at a voltage above the plateau value, the combined rates for these counters was large compared to the beam rate. Small differences in the timing in the electronics for the 20 veto scintillators (4 A, 4 A' and 12 B's) cause the signal going to the event definition to cut the event. This time window was measured (≈ 60 ns) and the effect of removing good events in this time window was calculated for all the targets. Because of this wide time window, and the high event rate for nuclear targets, this correction turned out to be rather large ($\sim 6\%$).

Table 4.4: Corrections to the data

| Type of correction | Al | Si | Ca | Mo | Sn | Pb |
|------------------------|-------|-------|-------|-------|-------|-------|
| Muon fraction | 0.94 | 0.95 | 0.95 | 0.88 | 0.92 | 0.92 |
| Capture fraction | 0.608 | 0.657 | 0.849 | 0.955 | 0.958 | 0.966 |
| Stop fraction | 0.91 | 0.73 | 0.88 | 0.81 | 0.83 | 0.82 |
| Prompt rejection | 1.00 | 1.02 | 1.019 | 1.006 | 1.014 | 1.016 |
| Target absorption | 1.24 | 1.13 | 1.21 | 1.15 | 1.165 | 1.208 |
| Stops in scintillators | 0.987 | 0.966 | 0.992 | 0.979 | 0.975 | 0.966 |
| Pion contamination | 0.998 | 0.998 | 0.998 | 0.998 | 0.998 | 0.994 |
| Cosmic background | 0.998 | 0.998 | 0.999 | 0.998 | 0.998 | 0.996 |
| Pileup | 0.985 | 0.985 | 0.985 | 0.985 | 0.985 | 0.985 |
| Random veto, A A' B | 1.068 | 1.060 | 1.052 | 1.065 | 1.076 | 1.048 |
| Random veto, cosmic | 1.01 | 1.01 | 1.005 | 1.02 | 1.008 | 1.005 |

- Various: smaller corrections were used to account for; possible random vetoing by trigger scintillators, random vetoing by the cosmic ray background chambers, and by the unlikely event of two muons arriving at the same time. All the corrections are listed in Table 4.4. A 24% loss is quoted as a 1.24 multiplying factor in the number of gammas, and a 1.3% contamination as a 0.987 factor.

4.4.3 Errors

There are errors associated with the corrections described in Table 4.4 and they are listed in Table 4.5. The most important ones are:

- Muon stops: To estimate this error when calculating the stop fraction different sets of ADC and TDC values were tried for cuts in the scintillators. The differences with the final stop fractions represented the error. These errors were of the order of 1.5% and represent one of the largest errors in the final calculations.

- **Target Absorption:** This error is mainly statistical and represented by the number of GEANT events generated. Photons were generated at different places in the target. In this way the error in the acceptance due to the unknown stopping distribution was estimated. Finally, although photons were generated in 10 MeV intervals, the acceptance was estimated assuming a typical RMC spectrum for all the targets. All these errors were added in quadrature for the total target absorption.

- **Energy calibration:** since the momenta of the pair particles are proportional to the magnetic field, one important contribution to the energy calibration error is due to the uncertainty in the field measurement. From the analysis of real data compared to Monte Carlo for a 7.1 kG field, it was determined that the error in the field was $\sim 0.5\%$. This agrees with the uncertainty in the magnetic field as extracted from the field maps. To estimate the effect this has in calculating the branching ratios, one shifts the energy spectra by this fraction and counts the total number of photons. Another source of error in the energy calibration is how well the thickness of the lead converter is known. The energy loss of the pair particles, as they leave the converter, is proportional to the thickness of the converter. One can change the thickness of the lead converter in GEANT to match the energy resolution measured. However this thickness cannot be determined to better than 0.01 mm, which is the error one finds when measuring the thickness at different places on the converter. By changing the thickness of the converter by this amount in the Monte Carlo simulation, one can estimate what error this represents in the energy calibration of the detector, and consequently in the acceptance.

- **Acceptance:** The minimum error on the acceptance is the 3.4% error on the weighted average for the three measurements of the π^-C used for normalization. The total error in the acceptance found by comparing the data to the Monte Carlo, was 4.2%. This includes the 3.4% error in the branching ratios used for normalization as well as the statistics in both, the data and the Monte Carlo. Although the photon spectrum from the π^-C radiative capture is centered around 120 MeV, unlike the smooth decay from 57 to 90 MeV for typical RMC spectra, the results indicated that the response function was understood quantitatively. For aluminum and silicon no theoretical spectra are available and one needs, in order to calculate their branching ratios, to make an intelligent guess as an input spectrum. By using the Primakoff [37] polynomial, (see Eq. 4.18), as the input spectra, one can assign an error to this guess, based on the χ^2 of the fits. The error quoted as polynomial corresponds to the error in the branching ratio when using the polynomial that gave the best χ^2 of the fit, and the one for which this χ^2 doubled.
- **Random veto:** one takes the vetoing time window and counts the number of events randomly cut at different times. The difference in the number of photons cut represents this error.
- **Special cases:** no random events were recorded that included the veto counter for any of the molybdenum runs. After all the RMC data had been recorded, an extra run, using a random trigger, was taken for each target. The stopping fractions derived from these R-rate events agreed with the results for data

Table 4.5: Contributions to the error in the branching ratio (%)

| Type of Error | Al | Si | Ca | Mo | Sn | Pb |
|--------------------------|------|------|------|------|------|------|
| Statistics | 2.5 | 2.0 | 1.8 | 2.4 | 2.6 | 3.2 |
| Capture fraction | 0.07 | 0.07 | 0.08 | 0.08 | 0.08 | 0.04 |
| Muon stops | 2.8 | 2.8 | 2.8 | 5.0 | 2.8 | 2.8 |
| Prompt rejection | 0.4 | 0.5 | 0.5 | 0.4 | 0.7 | 1.1 |
| Target absorption | 3.0 | 3.0 | 3.0 | 3.0 | 3.0 | 3.0 |
| Stops in scintillators | 0.6 | 1.5 | 0.4 | 1.0 | 1.3 | 1.7 |
| Random A A' B veto | 0.6 | 0.5 | 0.4 | 0.7 | 0.6 | 0.8 |
| Pion contamination | 0.05 | 0.05 | 0.05 | 0.05 | 0.05 | 0.05 |
| Cosmic background | 0.04 | 0.03 | 0.02 | 0.03 | 0.04 | 0.08 |
| Random veto, cosmic | 0.25 | 0.2 | 0.25 | 0.6 | 0.2 | 0.2 |
| Polynomial (k_{max}) | 6.0 | 6.0 | - | - | - | - |
| Energy calibration | 4.7 | 4.8 | 4.8 | 4.9 | 5.4 | 5.6 |
| Total | 9.1 | 9.1 | 6.6 | 8.1 | 7.4 | 8.0 |

taken earlier. For molybdenum the stopping fraction quoted corresponds to the later measurement, and one has no way to tell if any physical conditions had changed.

4.5 Branching Ratios

Branching ratios for all six targets were found. For aluminum and silicon, input spectra were derived from a polynomial of the form,

$$\frac{dG(x)}{dk} \sim (1 - 2x + 2x^2)x(1 - x)^2 \quad \text{with } x = \frac{E}{E_{max}} \quad (4.18)$$

where E is the photon energy. This polynomial was first derived by Primakoff [37] and represents the RMC spectrum when one considers only the muon radiating term, which accounts for almost 60% of the total RMC spectrum. Different input spectra are generated with this polynomial for different E_{max} values. These inputs are folded with the detector response function and compared to the real data. The

one that gives the best fit, minimum χ^2 , was used as the input. A comparison between the silicon data and the folded spectrum from the polynomials with $E_{max} = 85, 87, 90, 92, 95$ MeV is shown in Figure 4.14. The best fit was obtained for $E_{max} = 92$ MeV. For aluminum, a best fit to the data was obtained when using a polynomial with $E_{max} = 90$ MeV, see Figure 4.13.

Two different methods will be used to find the branching ratios for each of the other 4 elements; the integral, and the fitting method. In the integral method, one sums all the gammas with energies over 57 MeV, for the data as well as for the predicted spectrum used. The experimental branching ratio is then

$$\left[\frac{RMC}{OMC} \right]_{exptal} = \left[\frac{RMC}{OMC} \right]_{predict} \times \frac{N_{exptal}^{\gamma}}{N_{predict}^{\gamma}}. \quad (4.19)$$

In the fitting method one uses the different theoretical spectra (convoluted by the response function) to fit the data, with the normalization of the theoretical spectrum as a free parameter. The theoretical branching ratio was then multiplied by the normalization factor to give the experimental one. If the shape of the data spectrum is well fit by the theoretical model, then the branching ratios obtained by both methods should be in close agreement. For ^{40}Ca spectral shapes from Gmitro *et al.* [2] and Christillin [1] were used. For the remaining three targets, molybdenum, tin, and lead, the spectral shapes and input branching ratios of Christillin *et al.* [26] were used.

4.5.1 $^{27}Al, ^{28}Si$

The best fit to the aluminum data was obtained for a Primakoff polynomial with $E_{max} = 90$ MeV ($\chi^2=0.88$). The chisquared of the fit almost doubled (~ 1.6) for the polynomials with $E_{max} = 85$ and $E_{max} = 95$. The fits are shown in Figure 4.13. The data resulted from 4.0×10^{10} muon stops (1651 photons with $E \geq 57$ MeV).

Table 4.6: Branching ratios for aluminum and silicon. Spectra fitted to polynomial

| Target | $G_{>57}(10^{-5})$ |
|----------|--------------------|
| Aluminum | 1.39 ± 0.13 |
| Silicon | 1.92 ± 0.17 |

The silicon data were best fitted to the Primakoff polynomial with $E_{max} = 92$ MeV, and the polynomial error was determined as in the aluminum case. The silicon data resulted from 3.8×10^{10} muon stops, (2501 photons with $E \geq 57$ MeV). The branching ratios for these targets are listed in Table 4.6.

4.5.2 ^{40}Ca

The branching ratios for ^{40}Ca have been measured in several previous experiments, and there exist theoretical models to compare with. The photon energy spectrum was compared to the theoretical spectra of Christillin [1] and Gmitro *et al.* [2]. All the theoretical spectra depend on g_p . In the integral method one uses the number of photons predicted for the different branching ratios, to find the branching ratio corresponding to the photons seen. In the fitting method one chooses the shape that best fits the data, to find the branching ratio scaling factor. In Figure 4.15 the spectra predicted by Gmitro, for the number of stops in this experiment, (3.4×10^{10} yielding 3,128 photons with $E \geq 57$ MeV), is folded with the response function and plotted together with the data for comparison. The best fit is obtained for $g_p/g_a = 7.5$. However neither this shape, nor the other two, could successfully fit the high energy end of the spectrum, $E \geq 80$ MeV. This results in a scaling factor that gives an area under the curve somewhat smaller than that

Table 4.7: Branching ratios for ^{40}Ca , for the integral and fitting methods

| Theory | $G_{>57}(10^{-5})$ | |
|-----------------|--------------------|-----------------|
| | integral | fitting |
| Gmitro [2] | 2.03 ± 0.13 | 1.91 ± 0.16 |
| Christillin [1] | 2.10 ± 0.14 | 2.03 ± 0.16 |

indicated by the experimental data. As a result, the branching ratios deduced in this way are lower than the ones obtained in the integral method.

In Figure 4.16 the data were compared to spectra predicted by Christillin. From Christillin's spectra, the integral method yielded a value for $g_p/g_a = 4.8 \pm 0.7$ (see Chapter 5). From the linear relationship between the input branching ratios, and the number of gammas predicted, one finds the branching ratio corresponding to the number of photons observed. In the fitting method one compares the shape of the four spectra provided (with $g_p/g_a = -6.8, 0.0, 6.8$ and 13.6) to the data. One interpolation to obtain input shapes for other spectra is highly suspect and was not attempted. The input corresponding to $g_p/g_a = 6.8$ gave the closest fit to the data. One can also compare the data to the Primakoff polynomial for different values of E_{max} . A best fit was obtained for E_{max} between 93 and 94 MeV, but again this smooth function fails to cover the region over 80 MeV. A summary of the branching ratios deduced by using both theories, from the integral and fitting method is presented in Table 4.7. Because of the fitting problems mentioned above, the values obtained using the fitting method are lower and less reliable than the ones obtained in the integral method.

4.5.3 Mo, Sn and Pb

The theory of Christillin *et al.* [26] was used for these three nuclei. For molybdenum, although the data are closer to the predicted spectra using either $g_p/g_a = 0$ or $g_p/g_a = -6.8$, the shape of the spectrum is best fitted to the spectra obtained with $g_p/g_a = 13.6$. As for ^{40}Ca , the predicted shapes fail to cover the high energy end of the spectrum, 75 to 85 MeV in this case. This is clear when comparing the data and the predicted spectra as display in Figure 4.19. The Primakoff polynomial that best fitted the data corresponded to $E_{max} = 90$ MeV. A total of 3.6×10^{10} stops yielded 1,859 photons with energy over 57 MeV. As in ^{40}Ca , the branching ratios obtained using the fitting method fail to include the high energy end of the spectrum and yield lower values than the ones obtained with the integral method. The branching ratios found are listed in Table 4.8.

The tin data, 3.8×10^{10} stops and 1,577 photons with $E \geq 57$ MeV, is shown in Figure 4.18. As for molybdenum, the data were closer to what is expected by using $g_p/g_a = -6.8$, however, all four spectra shapes fit the data equally well. A fit to the Primakoff polynomial yielded an $E_{max} = 87$ MeV. The branching ratios obtained in both, integral and fitting methods, are listed in Table 4.8.

The lead data were recorded in two different run periods. From the analysis of the random gate events in the data, the stop and muon fractions were derived. These fractions did change for both periods due to different conditions such as tuning of the RF separator. However, both data sets yielded very similar RMC rates, providing a good consistency check of the analysis. A total of 5.5×10^{10} stops, yielded 1,204 photons with $E \geq 57$ MeV. A comparison between the data and the spectra of Christillin [26], is shown in Figure 4.17. A lower RMC yield is found than what is predicted by the theory, for any of the four values of g_p . The spectral shape

Table 4.8: RMC branching ratios for Mo, Sn, and Pb. The theory of Christillin *et al.* [26] is used. The E_{max} for the Primakoff polynomial that give the best fit to the data are listed.

| Target | $G_{>57}(10^{-5})$ | | Polynomial | |
|------------|--------------------|-----------------|------------|----------|
| | integral | fitting | E_{max} | χ^2 |
| Molybdenum | 1.30 ± 0.11 | 1.18 ± 0.11 | 90 | 0.84 |
| Tin | 1.00 ± 0.08 | 0.98 ± 0.09 | 87 | 1.06 |
| Lead | 0.60 ± 0.05 | 0.57 ± 0.05 | 84 | 0.82 |

corresponding to $g_p/g_a = 0$ gives the best fit to the data. The Primakoff polynomial that best fits the data employs an $E_{max} = 84$ MeV. The branching ratios are listed in Table 4.8.

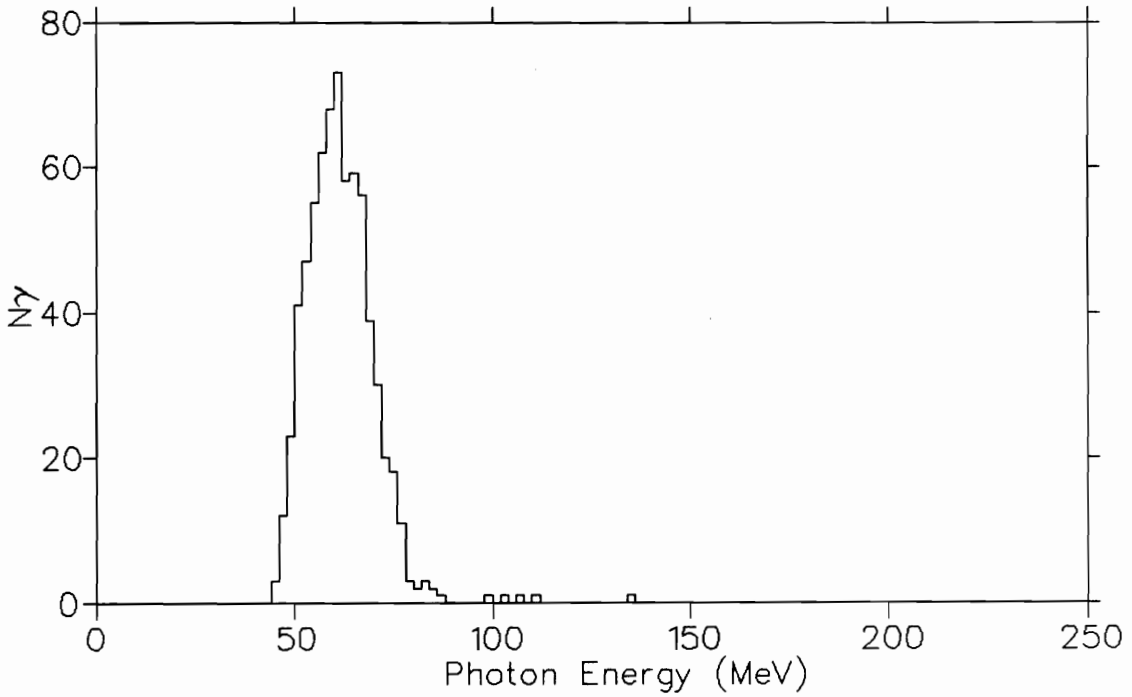
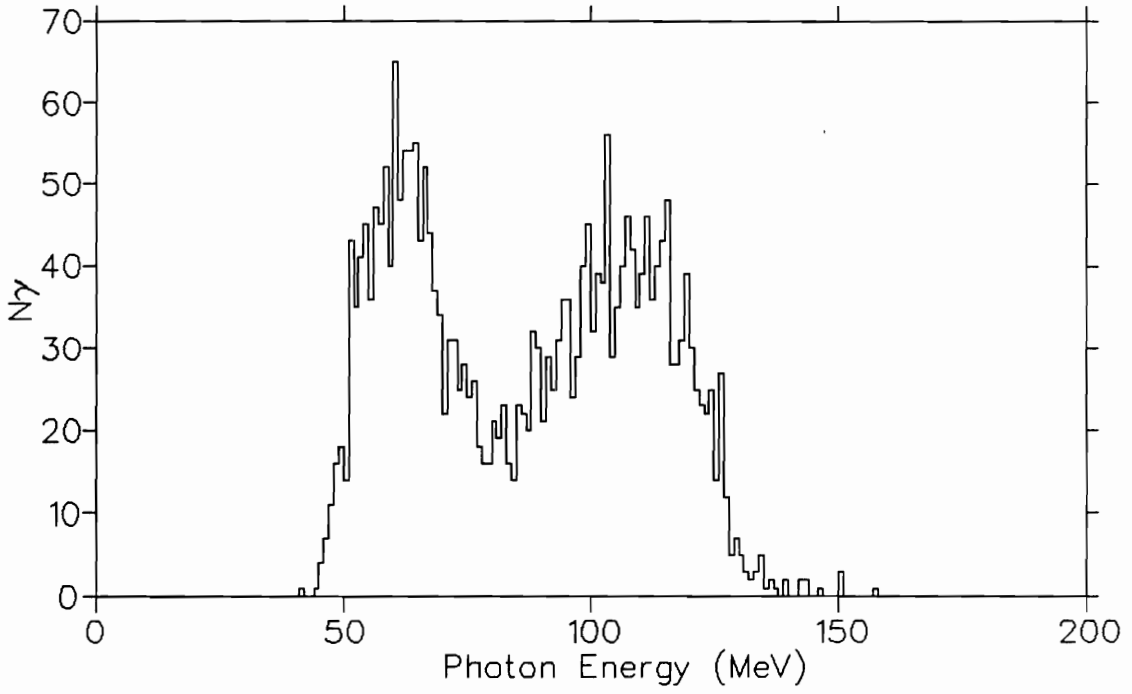


Figure 4.3: RMC in lead. Top: before any cuts showing radiative pion capture events. Bottom: after all cuts

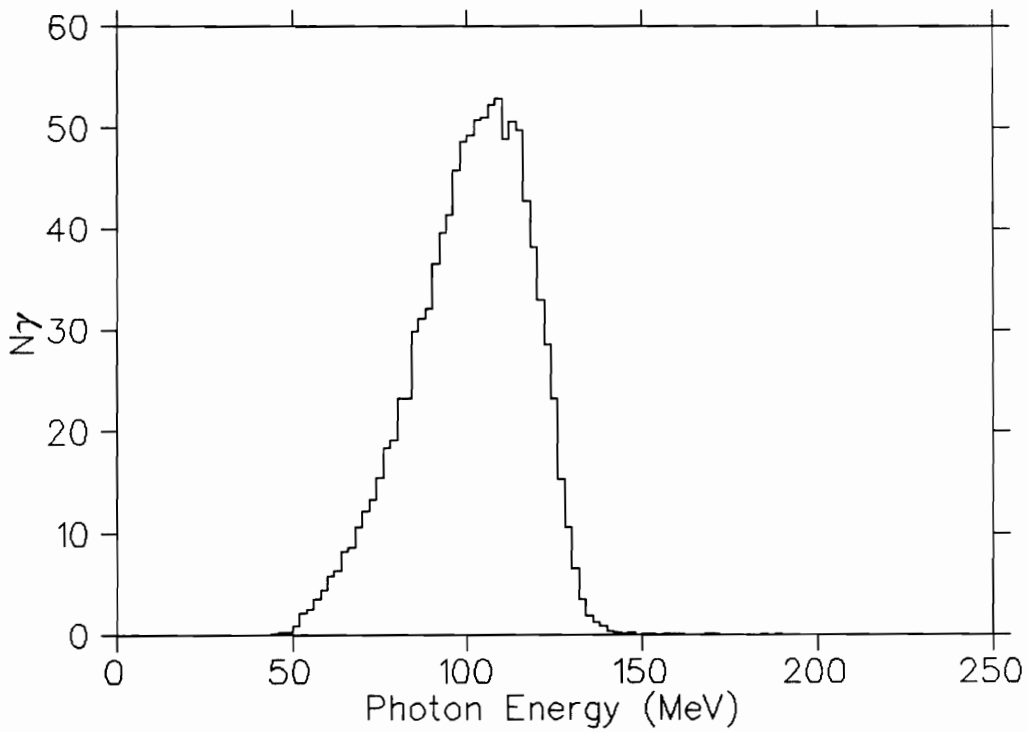
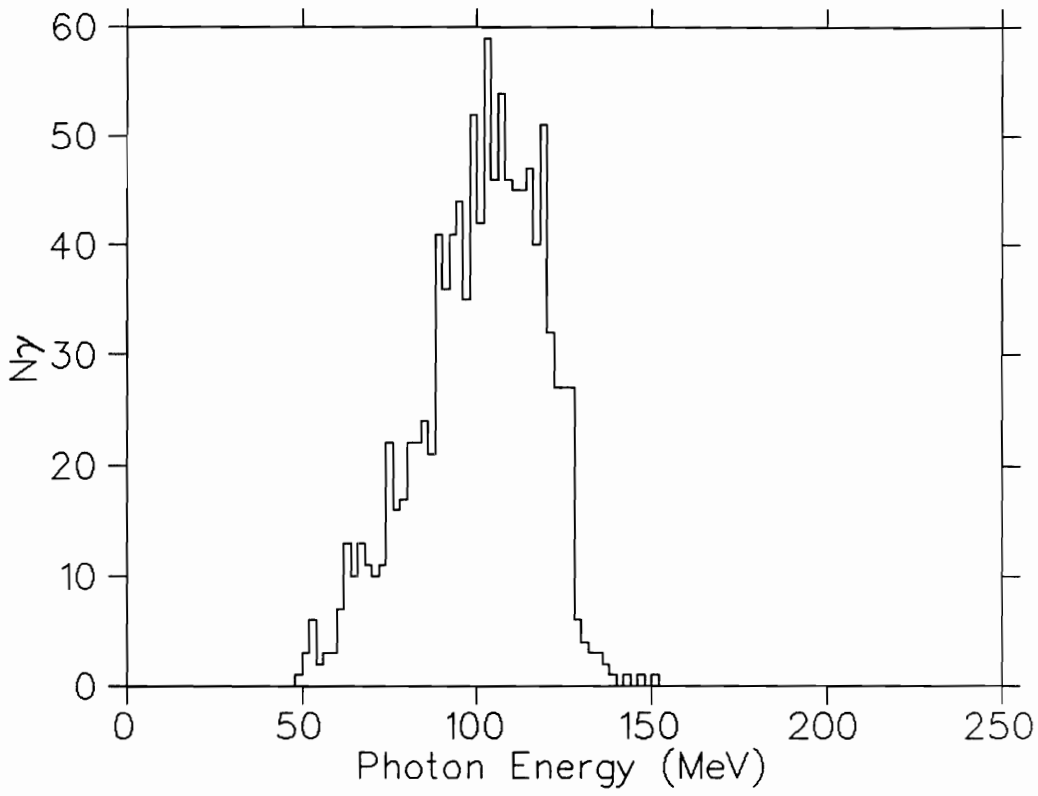


Figure 4.4: Comparison between events rejected as prompt and the corresponding radiative pion capture spectrum

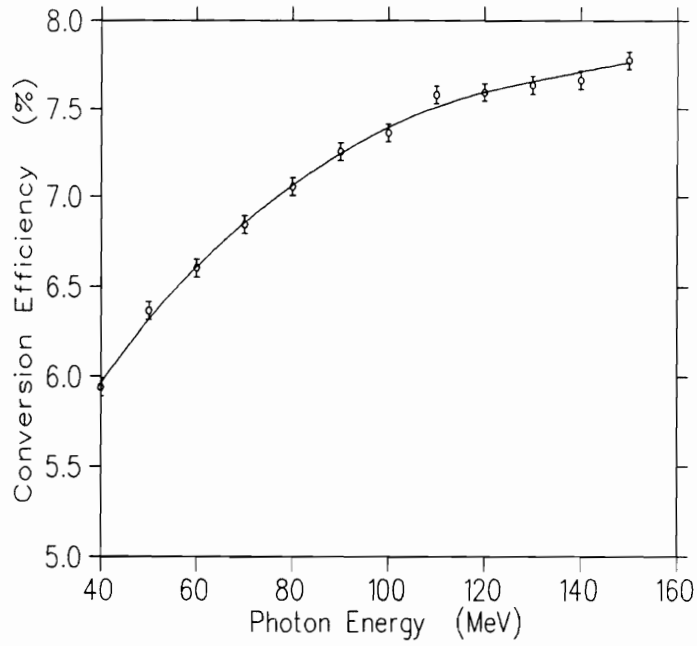


Figure 4.5: Probability of photoconversion in lead, for 1.0 mm converter

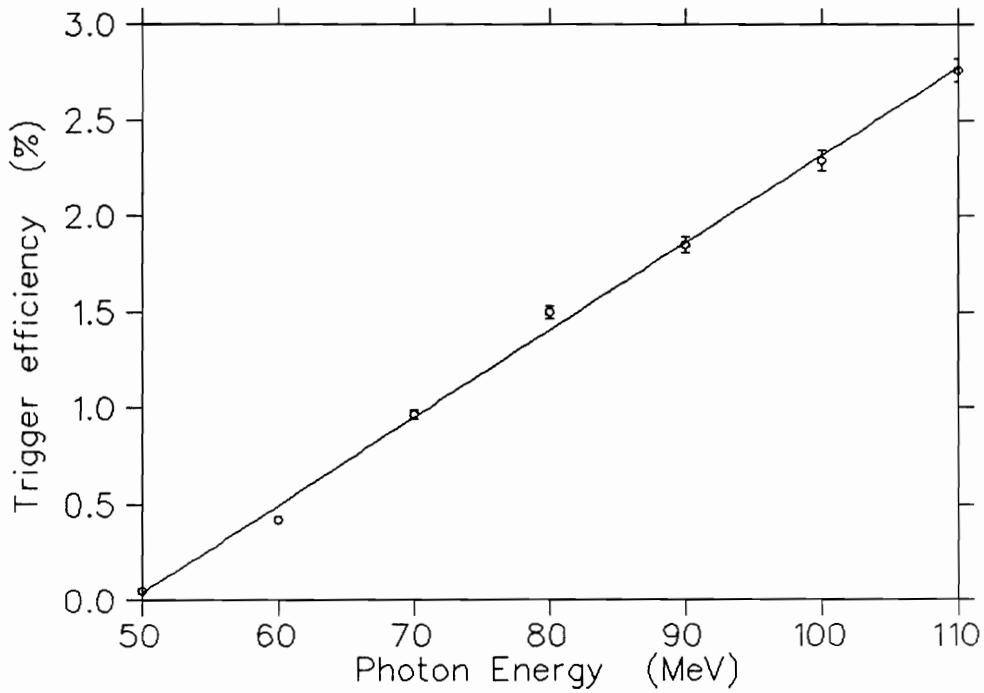


Figure 4.6: Photon trigger efficiency, calculated in GEANT

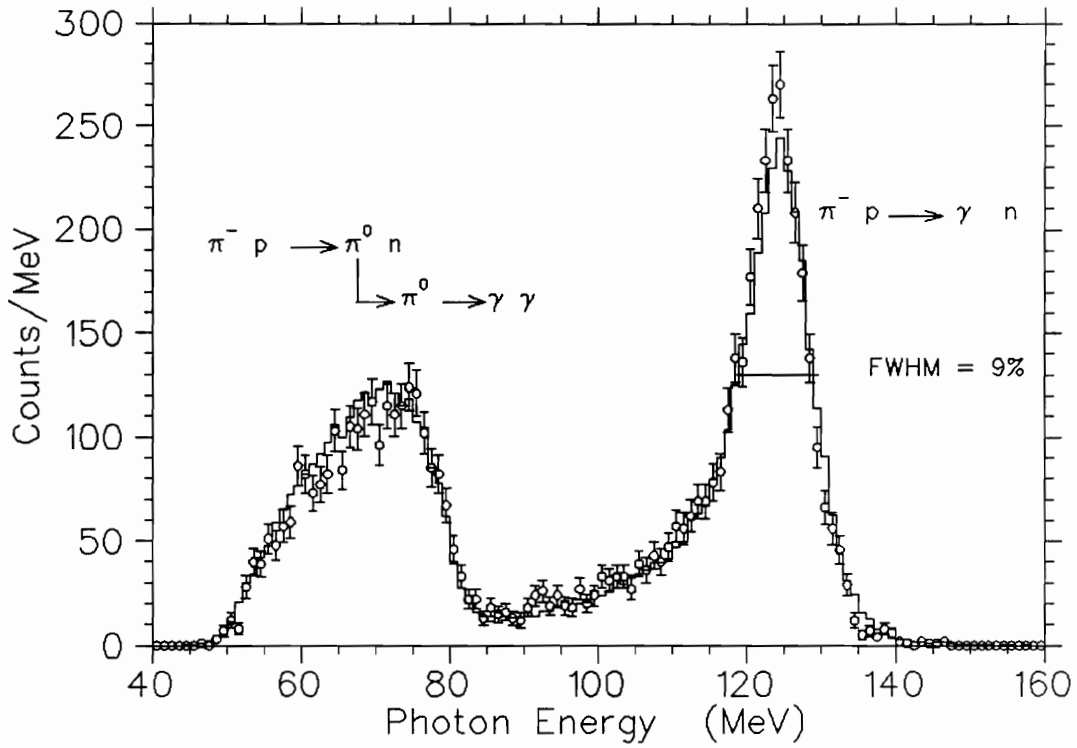


Figure 4.7: Radiative pion capture in hydrogen. Histogram: Geant data, points: experimental

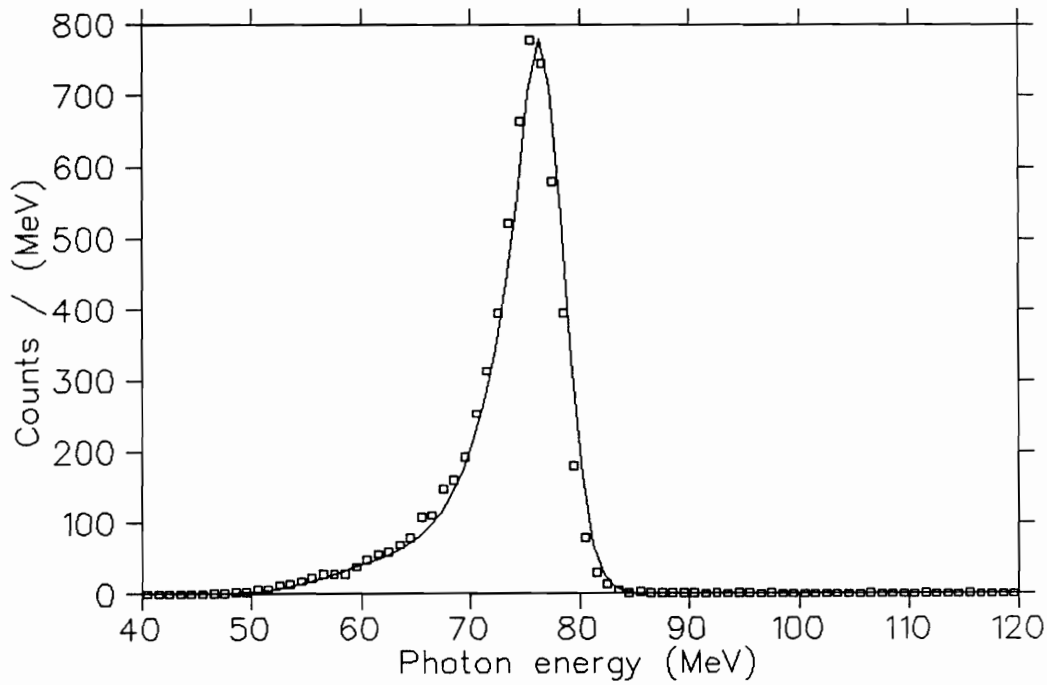


Figure 4.8: Energy resolution for 80 MeV photons. Response function (curve) compared to Monte Carlo data (points)

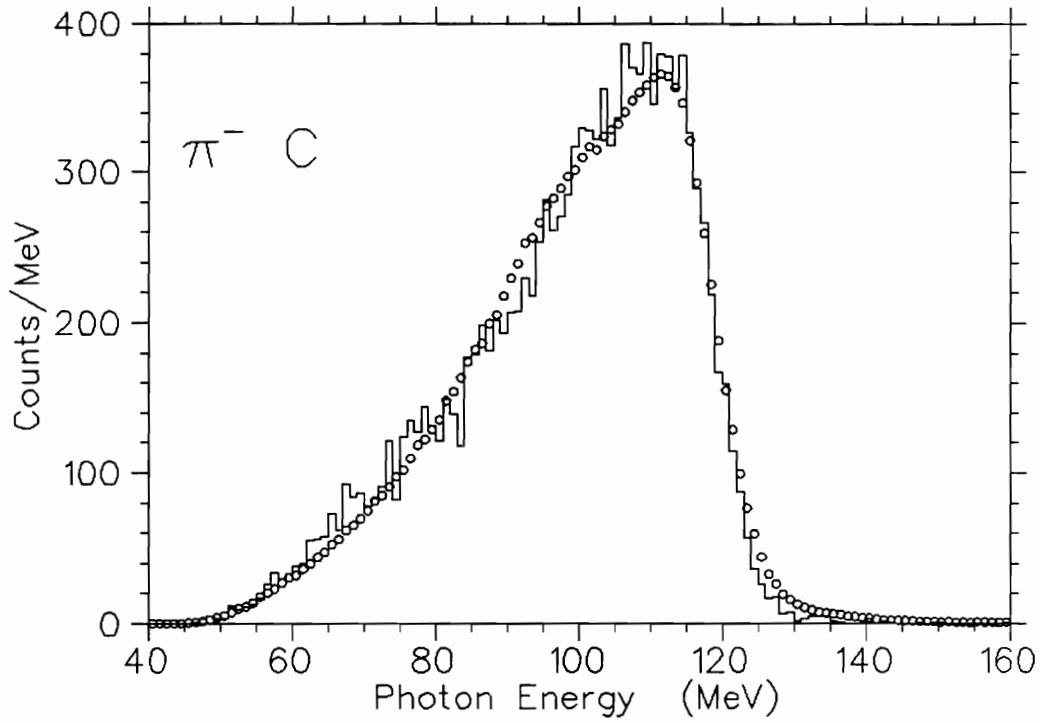


Figure 4.9: Radiative pion capture in ^{12}C . Comparison between Monte Carlo (points), and real data (histogram)

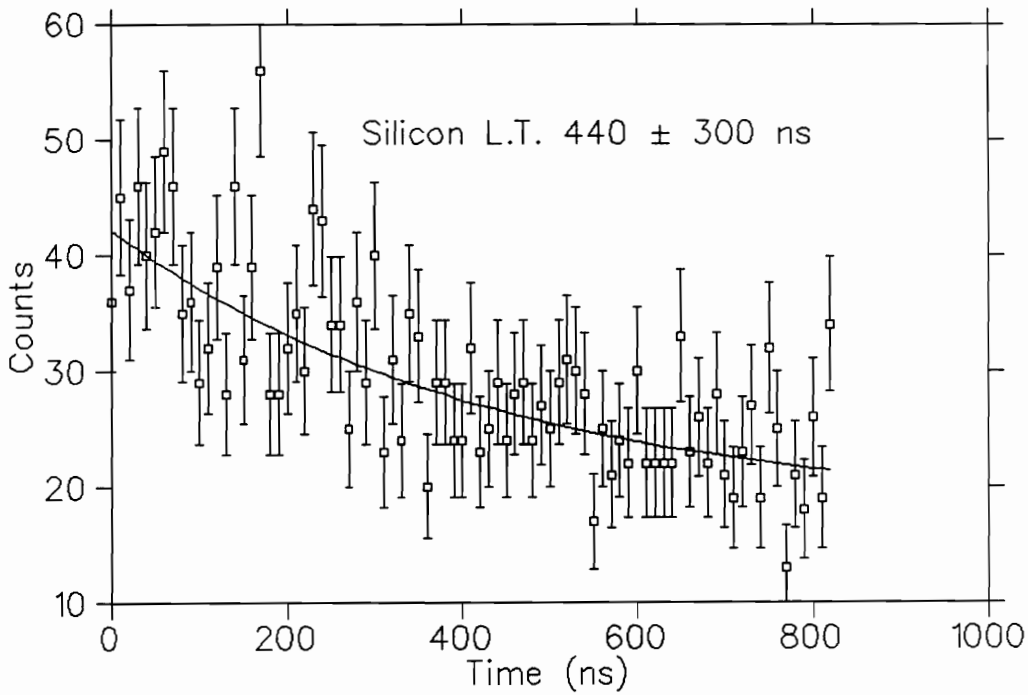


Figure 4.10: Time distribution of photon events for silicon

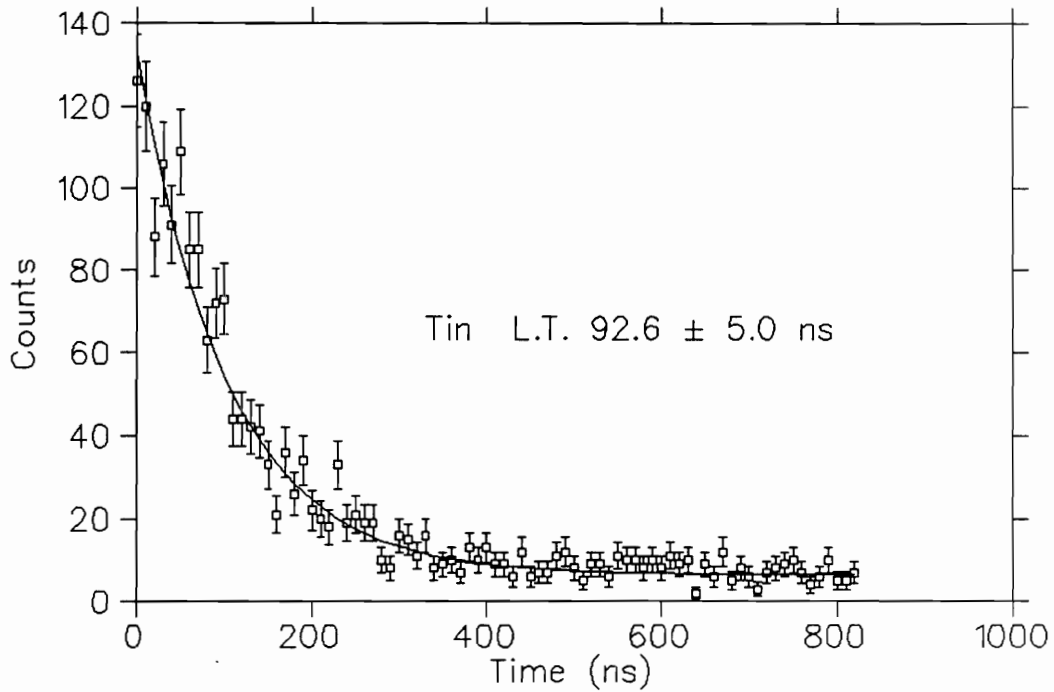
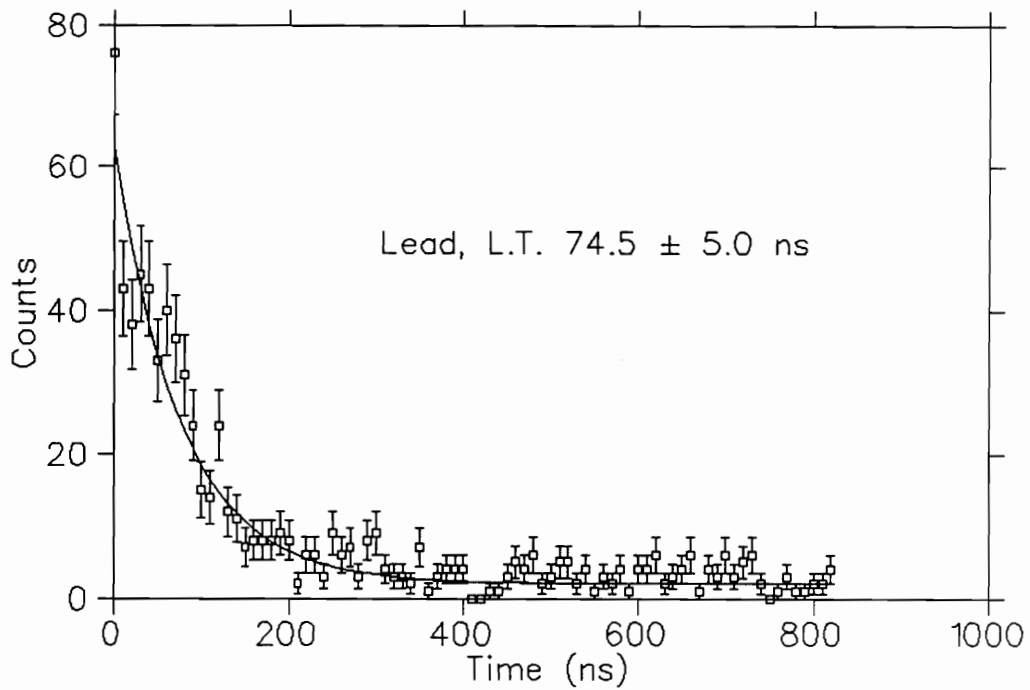


Figure 4.11: Time distribution of photon events for lead and tin

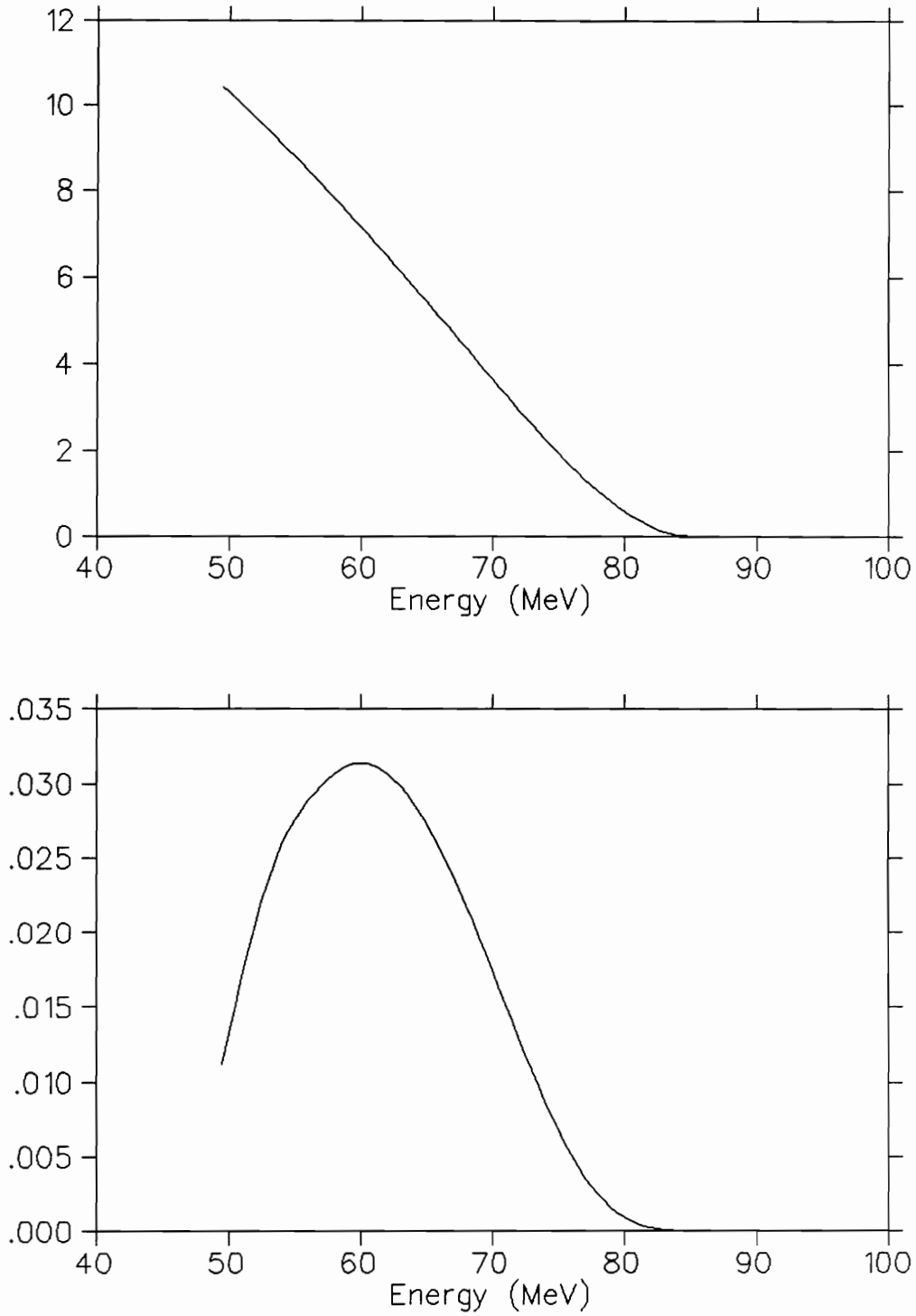


Figure 4.12: Top: input spectrum, bottom: same input after folded by response function

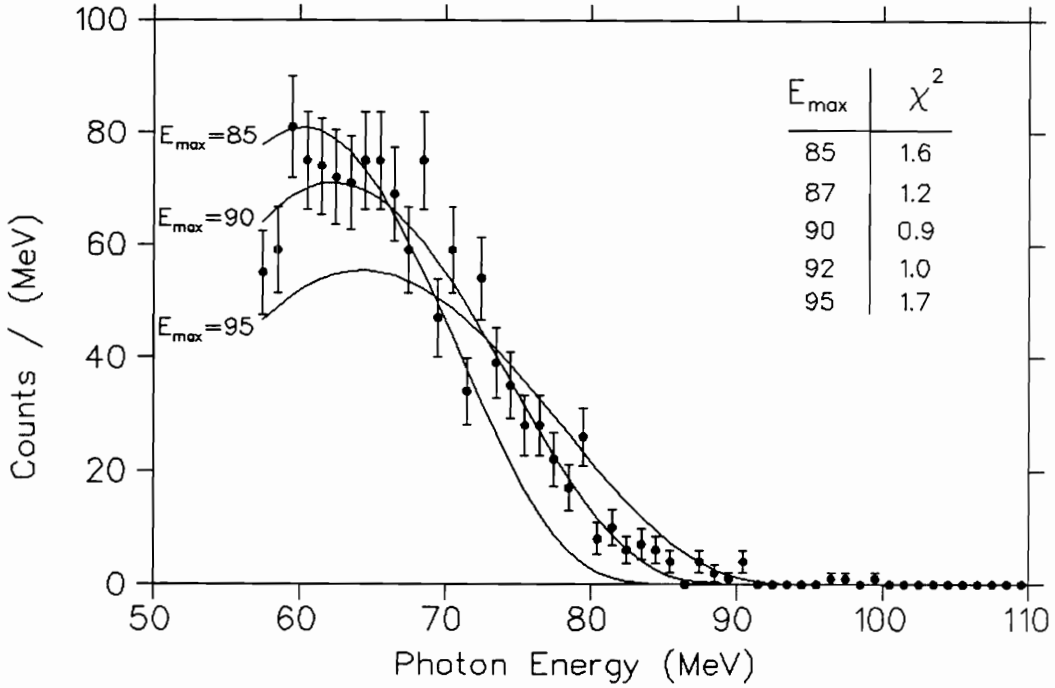


Figure 4.13: Comparison between polynomial with $E_{max}=85,90,95$ MeV, and the aluminum data

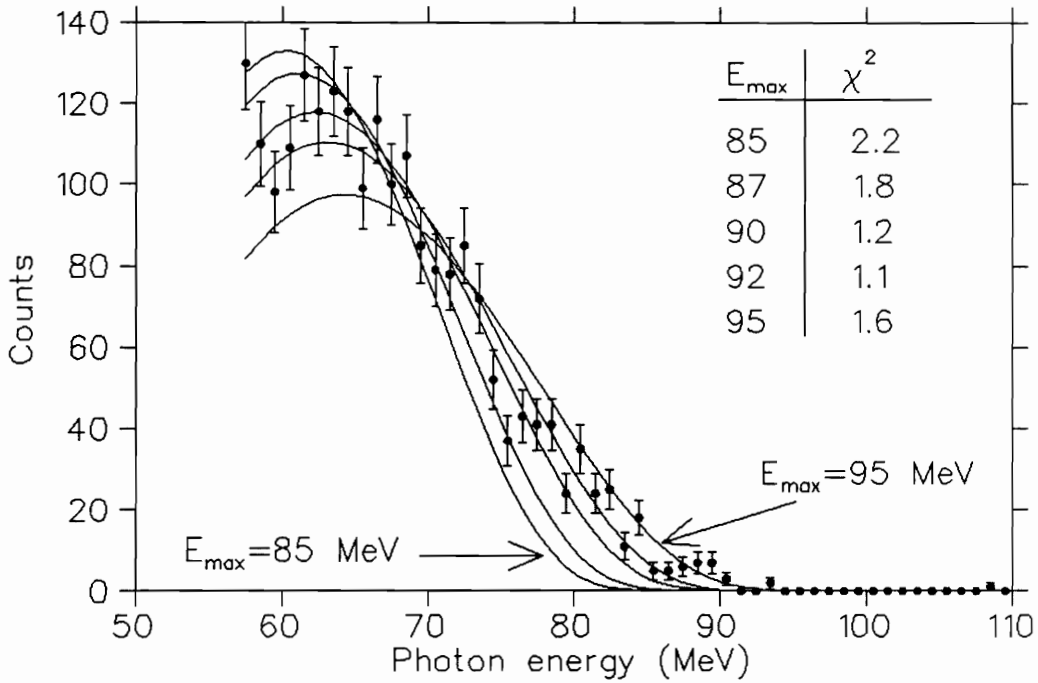


Figure 4.14: Comparison between polynomial with $E_{max}=85,87,90,92,95$ MeV, and the silicon data

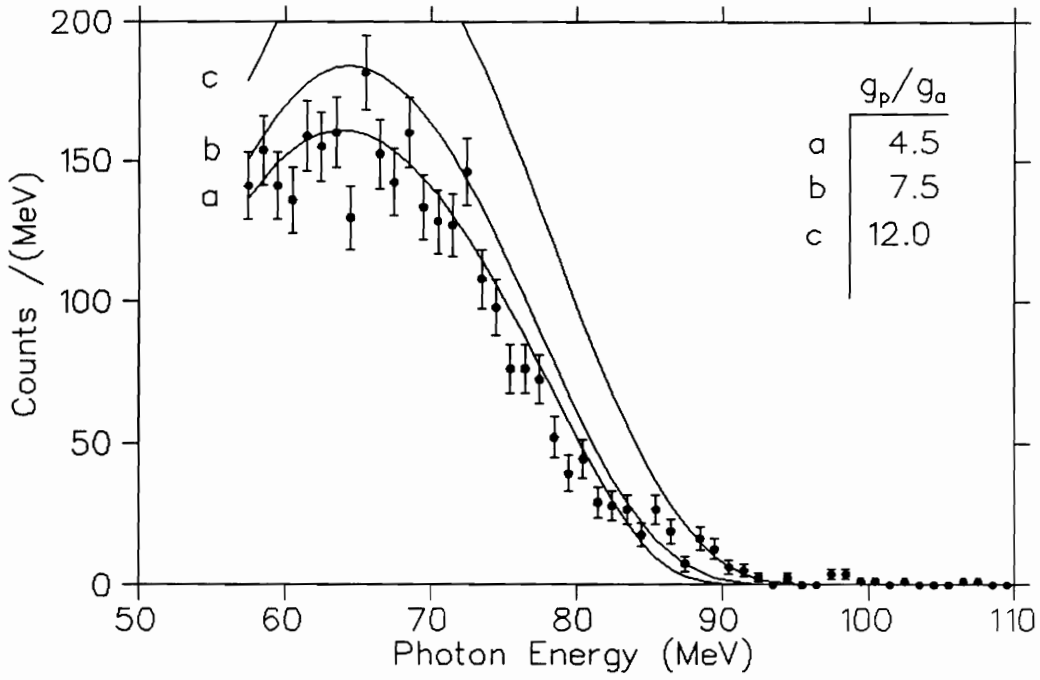


Figure 4.15: Photon energy spectrum for ^{40}Ca compared to Gmitro *et al.*[2]

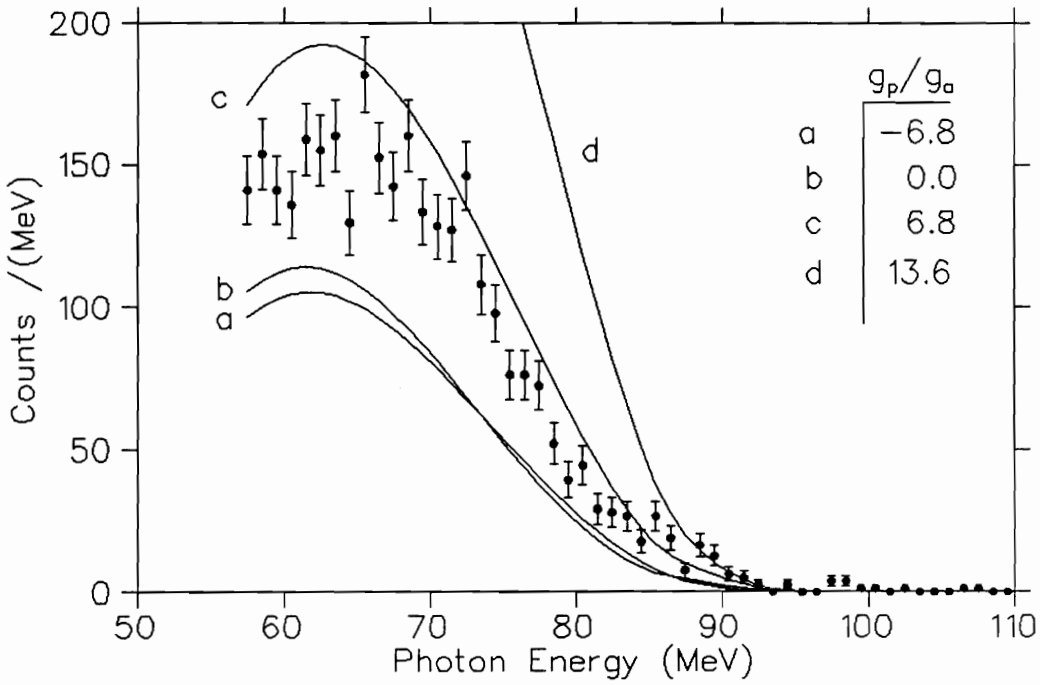


Figure 4.16: Photon energy spectrum for ^{40}Ca compared to Christillin *et al.*[1]

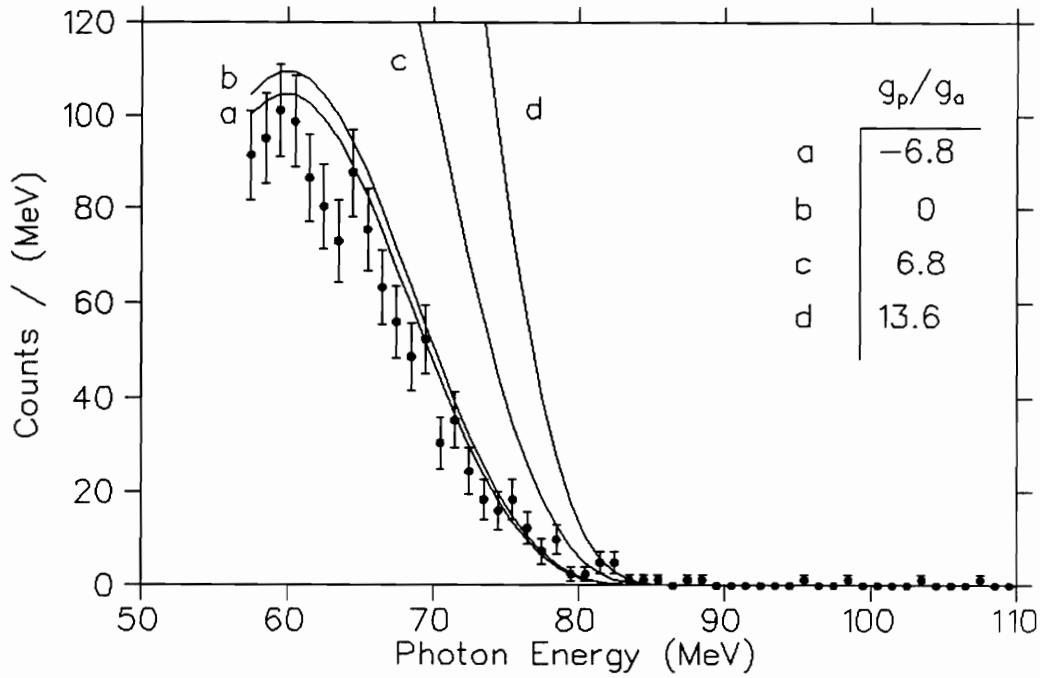


Figure 4.17: Photon energy spectrum for Pb compared to Christillin *et al.*[26]

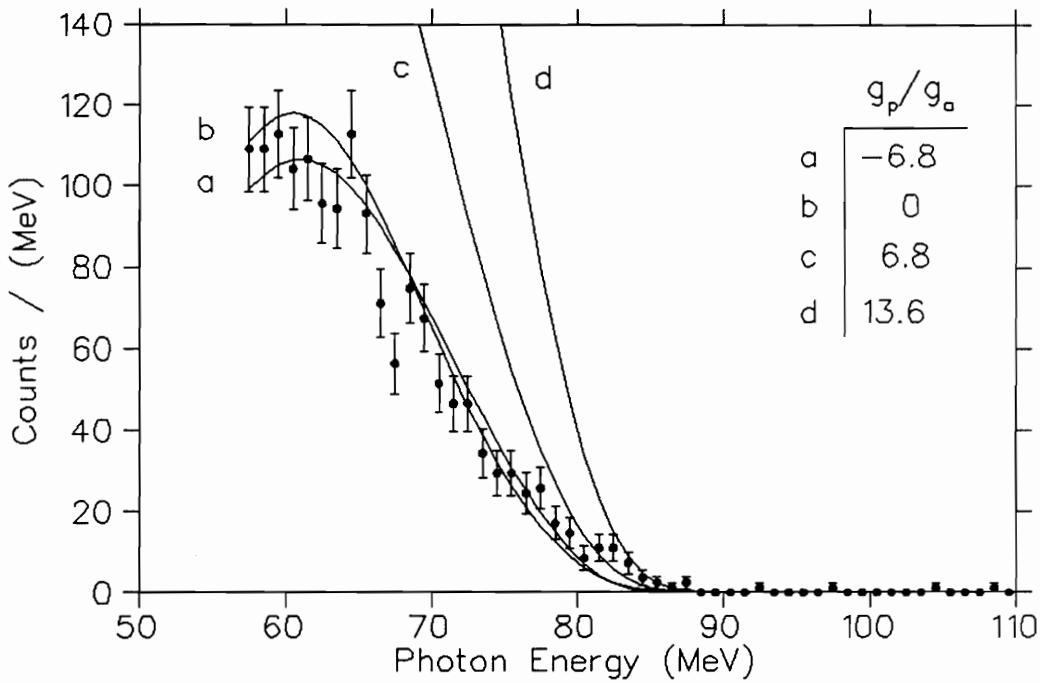


Figure 4.18: Photon energy spectrum for Sn compared to Christillin *et al.*[26]

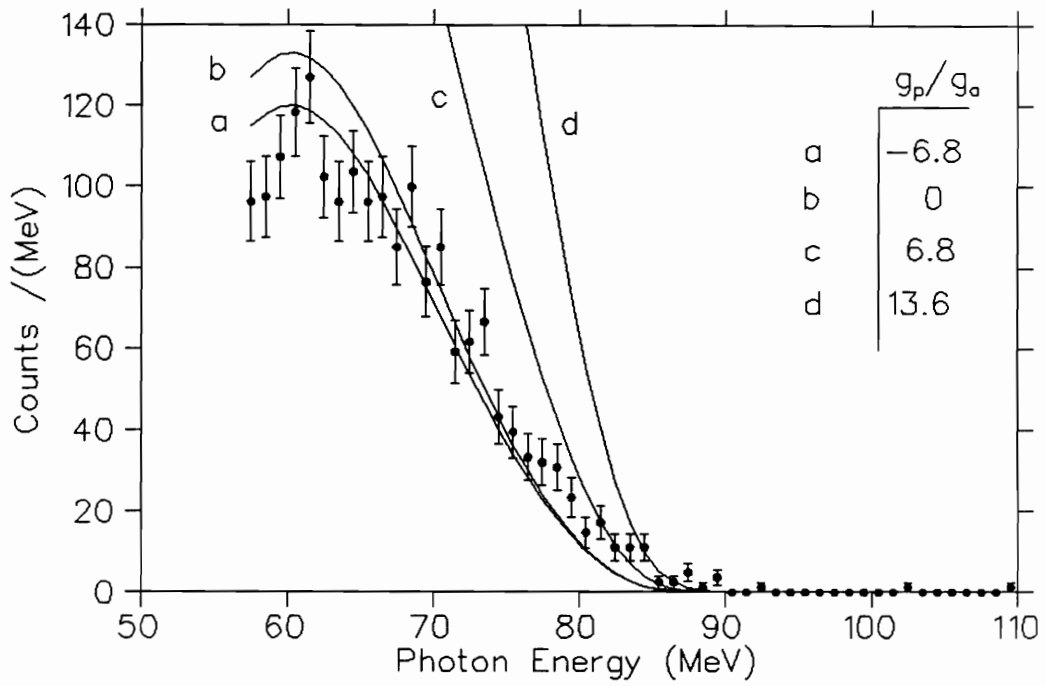


Figure 4.19: Photon energy spectrum for Mo compared to Christillin *et al.*[26]

Chapter 5

Results and Conclusions

5.1 Results

5.1.1 Al, Si

There has been another RMC measurement in Al by Döbelli *et al.* [3]. In their branching ratio calculation they used the Primakoff polynomial to fit the data. Their value, $(1.83_{-0.25}^{+0.58}) \times 10^{-5}$, is 2σ higher than what is found in this work. In Döbelli's experiment it could not be ruled out that the data had been taken with a thinner target than was used in calibration measurements. A thinner target not only affects the stopping fraction but the photo conversion in the target as well. In their simulation of the target absorption they generated photons with an average energy of 70 MeV which does not represent the RMC energy spectrum very well.

There have been no measurements for RMC in silicon and one can only report the measured branching ratio. If one suspects that two neighbor nuclei such as $^{27}_{13}\text{Al}$ and $^{28}_{14}\text{Si}$, should not yield different RMC branching ratios, then the branching ratios measured clearly contradict this view. However if one thinks of the RMC rates in terms of the difference between the number of neutrons and protons, then a branching ratio for silicon, $N = Z$, does not have to agree with aluminum's. Since there is no model to predict these branching ratios in terms of g_p , then one can not infer a g_p value from these results. Döbelli *et al.* [3] extrapolated Christillin's Fermi gas model calculation to predict the theoretical branching ratios for targets

for which no calculation had been performed. This method relies on assuming a linear relationship between the RMC branching ratios and the atomic number Z , and that one can extend a Fermi gas model for medium-heavy nuclei to light nuclei. The Z dependence, although visually appealing if one displays the known RMC branching ratios versus Z , ignores other physical quantities known to be crucial in RMC calculations. These include maximum momentum transfer, E_{max} , and α where $\alpha = (N - Z)/A$. To extend the Fermi gas model to light nuclei and to extract g_p from branching ratios predicted in this way is highly suspect.

5.1.2 ^{40}Ca

Several measurements and calculations have been performed for ^{40}Ca . A summary of these measurements is listed in Table 5.1. Theoretical spectra are presented for several values of g_p . From these the total number of photons is predicted. A polynomial fit to these points allows the extraction of the number of photons for any value of g_p . However, due to the slow variation of N_γ with g_p , a large error in g_p is obtained. Figure 5.1 shows the data compared to the theories of Gmitro *et al.* [2] and Christillin [1]. In the latter case the value of $g_p/g_a = -6.8$ was not used.

The results of this work are in good agreement with the existing data. Averaging the results of the experiments listed in Table 5.1 gives the value

$$G_{\geq 57} = (2.13 \pm 0.07) \times 10^{-5} \quad (5.1)$$

The values obtained for g_p/g_a from both theories are not identical due to the different spectral shapes used in both theories. It should be pointed out that

Table 5.1: Summary of RMC results for ^{40}Ca from recent measurements. The partial branching ratio $G_{>57}$ is given in units of 10^{-5} . For theories using the closure approximation, the value of E_{max} found is given. ‘RYY’ refers to the theory of Rood, Yano and Yano [38], ‘Chr’ refers to the theory of Christillin [1], ‘GOT’ refers to the theory of Gmitro *et al.* [2]

| $G_{>57}$ (10^{-5}) | Theory | E_{max} (MeV) | # events | g_p/g_a | reference |
|---|--------|--------------------|----------|--|---------------------------------|
| 2.11 ± 0.14 | RYY | 86.5 ± 1.9 | 1229 | 6.5 ± 1.6 | Hart <i>et al.</i> [39,40] |
| 2.07 ± 0.20 | — | — | 2450 | — | Frischknecht <i>et al.</i> [41] |
| 1.92 ± 0.20 | RYY | 90.8 ± 0.9 | ” | 3.5 ± 1.3 | ” |
| 1.96 ± 0.20 | Chr | — | ” | 4.6 ± 0.9 | ” |
| $2.35 \begin{smallmatrix} +0.32 \\ -0.30 \end{smallmatrix}$ | Chr | — | 3133 | 7.6 ± 1.6 | Virtue <i>et al.</i> [42] |
| $2.15 \begin{smallmatrix} +0.27 \\ -0.26 \end{smallmatrix}$ | GOT | — | ” | $6.0 \begin{smallmatrix} +2.8 \\ -2.9 \end{smallmatrix}$ | ” |
| 2.30 ± 0.21 | Chr | — | 3234 | $6.3 \begin{smallmatrix} +1.0 \\ -1.5 \end{smallmatrix}$ | Döbeli <i>et al.</i> [3,43] |
| 2.18 ± 0.16 | Chr | — | 3458 | 5.7 ± 0.8 | Armstrong <i>et al.</i> [27] |
| 2.04 ± 0.14 | GOT | — | ” | $4.6 \begin{smallmatrix} +1.7 \\ -1.8 \end{smallmatrix}$ | ” |
| 2.10 ± 0.14 | Chr | — | 3128 | 4.8 ± 0.7 | this work |
| 2.03 ± 0.13 | GOT | — | ” | 4.5 ± 1.5 | ” |

Christillin presents his results in terms of Δ , taking $\Delta = 1$ for the G-T value. Some authors have used $\Delta = 1$ as $g_p/g_a = 7.0$. A detailed explanation of previous RMC experiments in ^{40}Ca can be found in D. Armstrong’s thesis [44] and a recent review is found in Armstrong *et al.* [27].

The results obtained for g_p/g_a are lower than the G-T values, but in agreement with previous data.

Although there exists data for the muon-photon spin asymmetry for RMC in ^{40}Ca , the experimental error in measuring this asymmetry is too large to provide a value of g_p of the same quality as is obtained from the branching ratio method.

In summary, by using the theories available that predict the RMC branching

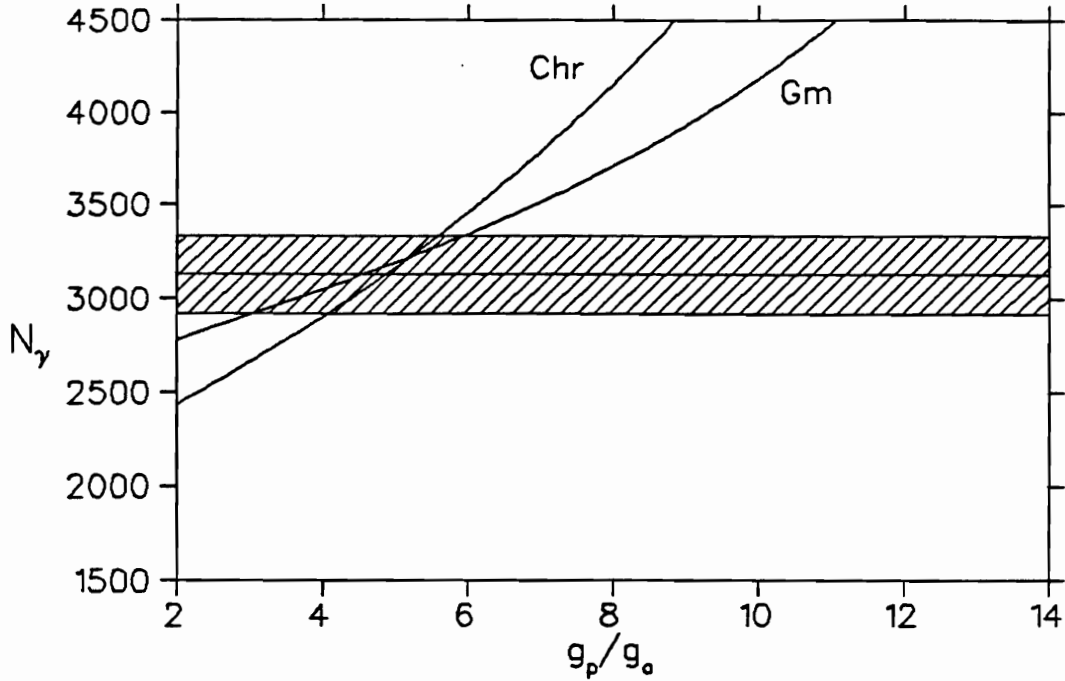


Figure 5.1: $N_{\gamma}^{\geq 57}$ from ^{40}Ca as a function of g_p/g_a for the theories of Christillin [1] ('Chr') and Gmitro *et al.* [2] ('Gm').

ratio in ^{40}Ca , in this work as well as in previous experiments, one obtains a smaller value of g_p than the G-T value.

5.1.3 Mo, Sn, and Pb

The branching ratios obtained for these three targets are all consistent with a value of $g_p = 0$. All the branching ratios fall under the predicted values for $g_p/g_a = 0$ and the extrapolation of the theory of Christillin *et al.* [26] is meaningless. However, a close examination of the branching ratios, together with the other three measurements, indicates an excellent agreement with the closure approximation presented by Christillin *et al.* [26], which was abandoned to perform a Fermi gas

Table 5.2: Predicted branching ratios using theory of Christillin *et al.* [26]

| Target | E_{max} | $1 - \alpha$ | Z | Poly Area | B.R. (10^{-5}) Closure | B.R. (10^{-5}) this work | Difference (%) |
|--------|-----------|--------------|----|-----------|----------------------------|------------------------------|----------------|
| Al | 90 | 0.963 | 13 | 0.727 | 1.45 | 1.39 ± 0.13 | + 4.3 |
| Si | 92 | 1.000 | 14 | 0.857 | 1.86 | 1.92 ± 0.17 | -3.1 |
| Ca | 93 | 1.000 | 20 | 1.000 | 2.05 | 2.07 ± 0.16 | - |
| Mo | 90 | 0.876 | 42 | 0.727 | 1.32 | 1.30 ± 0.11 | +1.5 |
| Sn | 87 | 0.843 | 50 | 0.553 | 0.90 | 1.00 ± 0.08 | -10.0 |
| Pb | 84 | 0.792 | 82 | 0.407 | 0.58 | 0.60 ± 0.05 | -3.3 |

model calculation,

$$R(x)dx \approx \frac{e^2 E_{max}^2}{\pi m_\mu^2} (1 - \alpha)x(1 - 2x + 2x^2)(1 - x)^2. \quad (5.2)$$

Using this expression to predict RMC rates in different nuclei, means that one uses as spectra the polynomial shapes for the appropriate element, and that the integrated rates depend only on E_{max} , α (the ratio between the difference and the sum of neutrons and protons), and the energy region available under the curve adopted. By using the E_{max} found from the polynomial fit to the data and the α factor for each element one can predict the different branching ratios. One may use the ^{40}Ca results as a normalization. The branching ratio for ^{40}Ca used is the one found by the polynomial fit to that data. Our results for the branching ratios obtained in this manner are listed in Table 5.2. The area under the polynomial curve is taken as 1.0 for ^{40}Ca , and the values quoted are as a fraction of the polynomial for $E_{max} = 93$ MeV used for ^{40}Ca . These areas represent the value after convolution with the detector's response function.

The E_{max} found is critical in this calculation. For instance the χ^2 to the fit to the Ca data when fitted to the polynomial with $E_{max} = 93$ MeV was 1.2939 and 1.2932 for $E_{max} = 94$ MeV. However, if the 94 MeV polynomial fit for the ^{40}Ca data was chosen, a branching ratio = 1.99×10^{-5} would had been obtained and the

branching ratios for the other targets would have deviated from the data by typically 15%.

The remarkable agreement with the data obtained by using the simple closure approximation, implies that as a first approximation, to predict the RMC/OMC branching ratios in different elements, all one needs to know is the maximum momentum transfer. This is the key to any RMC calculation. Due to the multiple contributing processes in a complex nuclei, such calculation is not trivial. Recently H. Fearing (private communication) has found that coulomb terms, previously ignored, could change the maximum momentum transfer in lead by as much as 19 MeV. In view of the difficulties in extracting the contribution due to the pseudoscalar coupling in complex nuclei, we believe little can be said about g_p from the branching ratios obtained for Al, Si, Mo, Sn, and Pb. These results, the total branching ratios as well as the spectral shapes, may provide some interesting hints to theorists since not only nuclei of different Z , but neighbor nuclei with different α , were studied.

5.2 Summary of RMC results

Data for RMC in light to heavy nuclei has been collected in two experiments, Döbelli *et al.* [3] and this experiment. In Figure 5.3 the comparison between the two experiments is shown. Only the aluminum branching ratios seem to fall outside the range of a naive interpolation between ^{40}Ca and lighter nuclei, ^{12}C and ^{16}O . If the same branching ratios are displayed versus α , Figure 5.2, then the aluminum branching ratio seems to follow the behaviour of all the other nuclei. All nuclei with $\alpha = 0$ seem to yield branching ratios very close to each other. These can be seen in tables 5.3 and 5.1.

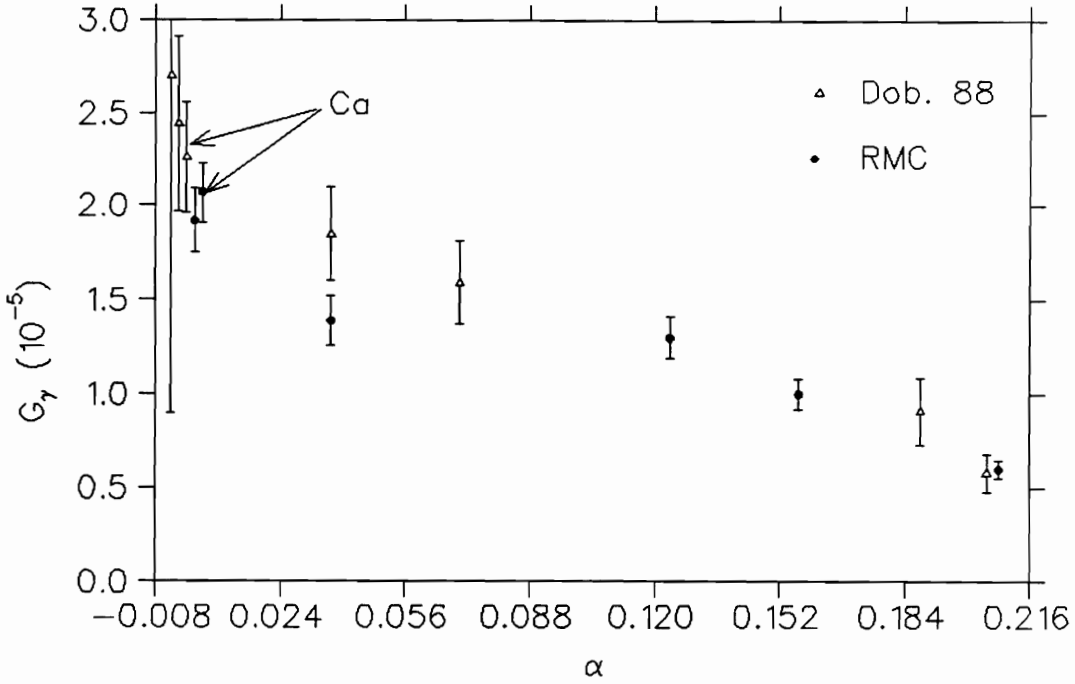


Figure 5.2: Comparison between Döbeli *et al.* [3] (Dob 88) and results in this work (RMC)

5.3 Suggestions for further work

One must have excellent, and well tested, theoretical models in order to extract the pseudoscalar coupling constant from RMC on complex nuclei. Therefore one should now concentrate on nuclei for which reliable predictions could be extracted.

Table 5.3: Summary of RMC branching ratios for $\alpha = 0$ nuclei.

| Element | $G_{>57}^\alpha (10^{-5})$ | Reference |
|------------------|----------------------------|---------------------------------|
| ^{12}C | 2.33 ± 0.17 | Armstrong <i>et al.</i> [27] |
| ^{12}C | 2.70 ± 1.80 | Döbeli <i>et al.</i> [3] |
| ^{16}O | 2.20 ± 0.22 | Armstrong <i>et al.</i> [27] |
| ^{16}O | 2.44 ± 0.47 | Döbeli <i>et al.</i> [3] |
| ^{16}O | 3.80 ± 0.40 | Frischknecht <i>et al.</i> [45] |
| ^{28}Si | 1.92 ± 0.17 | this work |
| ^{40}Ca | 2.13 ± 0.07 | world average |

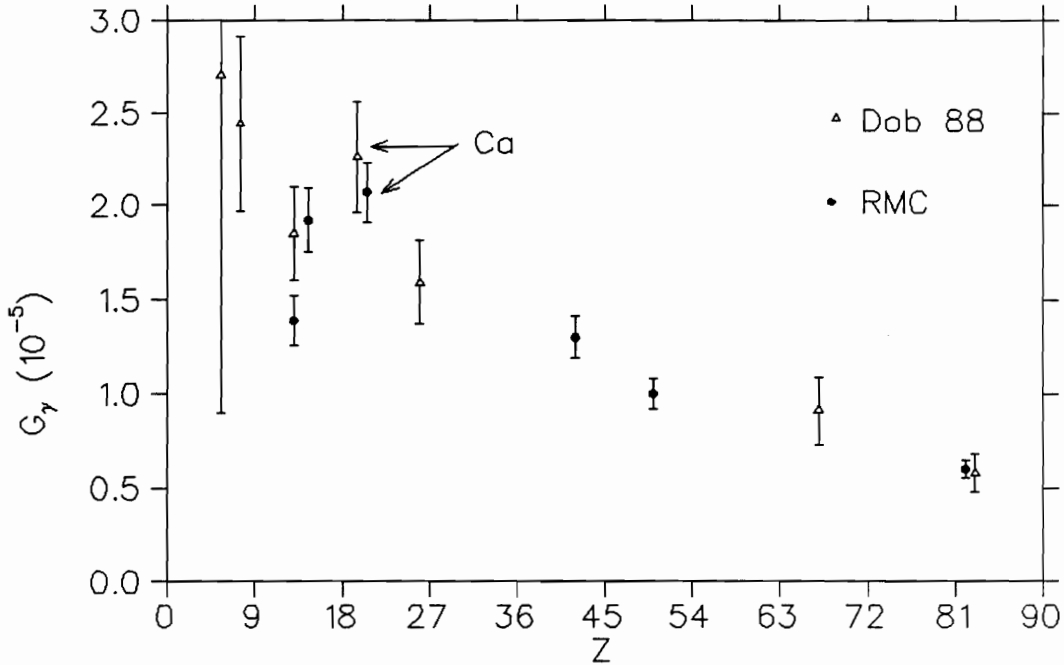


Figure 5.3: Comparison between RMC branching ratios ($E \geq 57$) for Döbeli *et al.* [3] (Dob. 88) and this work (RMC). Nuclei with $\alpha = 0$ were displaced for comparison.

Because of the extensive effort in calculating RMC in ^{40}Ca , it will be ideal to study any of its isotopes to test our understanding of this process. There is already OMC data available for ^{44}Ca , by Suzuki *et al.* [35]. Any difference in the RMC branching ratios for these targets cannot be blamed on coulomb effects, and no Z dependence should exist. There is also OMC data for three nickel isotopes, ^{58}Ni , ^{60}Ni , and ^{62}Ni and four chromium isotopes, ^{50}Cr , ^{52}Cr , ^{53}Cr and ^{54}Cr . Again, no Z dependence should be seen in the RMC rates for any of these isotopes. Additionally, the OMC rates for all the isotopes mentioned have been recently calculated by Chiang *et al.* [46], using a relativistic Fermi gas model and a local density approximation. Some problems encountered during this experiment have already been solved, and the RMC detector at TRIUMF could easily be used to measure RMC in other targets.

Bibliography

- [1] P. Christillin. *Nucl. Phys.*, **A362**:391, (1981).
- [2] M. Gmitro, A.A. Ovchinnikova, and T.V. Tetereva. *Nucl. Phys.*, **A453**:685, (1986).
- [3] M. Dobeli, M. Doser, L. van Elmbt, M.W. Schaad, P. Truol, A. Bay, J.P. Perroud, J. Imazato, and T. Ishikawa. *Phys. Rev. C*, **37**:1633, (1988).
- [4] E. Fermi. *Z. Physik*, **88**:161, (1934).
- [5] S. Glashow. *Nucl. Phys.*, **22**:579, (1961).
- [6] S. Weinberg. *Phys. Rev. Lett.*, **19**:1264, (1967).
- [7] A. Salam. *Elementary Particle Physics (Nobel Symp. No. 8)*, page 367. Almqvist and Wilsell, Stockholm, (1968).
- [8] T.P. Cheng and L.F. Li. *Gauge Theory of elementary particle physics*. Oxford University Press, (1984).
- [9] G. Bardin, J. Duclos, A. Magnon, J. Martino, A. Richter, E. Zavattini, A. Bertin, M. Piccinini, A. Vitale, and D. Measday. *Nucl. Phys.*, **A352**:365, (1981).
- [10] E.J. Bleser, L.M. Lederman, J. Rosen, J. Rothberg, and E. Zavattini. *Phys. Rev. Lett.*, **8**:288, (1962).
- [11] J.E. Rothberg, E.W. Anderson, E.J. Bleser, L.M. Lederman, S.L. Meyer, J.L. Rosen, and I.T. Wang. *Phys. Rev.*, **132**:2664, (1963).
- [12] A. Alberigi Quaranta, A. Bertin, G. Matone, F. Palmonari, G. Torelli, P. Dalpiaz, A. Placci, and E. Zavattini. *Phys. Rev.*, **177**:2118, (1969).
- [13] V.M. Bystrikskii, V.P. Dzhelepov, G. Chemnitz, V.V. Filchenkov, B.A. Khomenko, N.N. Khovansky, A.I. Rudenko, and V.M. Suvorov. *Sov. Phys. JETP*, **39**:19, (1974).
- [14] G. Bardin, J. Duclos, A. Magnon, J. Martino, A. Richter, E. Zavattini, A. Bertin, M. Piccinini, and A. Vitale. *Phys. Lett.*, **104B**:320, (1981).
- [15] H.P.C. Rood and H.A. Tolhoek. *Nucl. Phys.*, **70**:658, (1965).

- [16] M. Gmitro and P. Truol. *Adv. Nucl. Phys.*, **18**:241, (1987).
- [17] P. Christillin and S. Servadio. *Nuovo Cim.*, **42 A**:165, (1977).
- [18] W-Y. P. Hwang. *Phys. Rev.*, **18C**:414, (1978).
- [19] W-Y. P. Hwang. *Phys. Rev.*, **C22**:233, (1980).
- [20] A. Wulschleger and F. Scheck. *Nucl. Phys.*, **A326**:325, (1979).
- [21] M. Gmitro and A.A. Ovchinnikova. *Nucl. Phys.*, **A356**:323, (1981).
- [22] Harold W. Fearing. *Phys. Rev.*, **C21**:1951, (1980).
- [23] Douglas S. Beder and Harold W. Fearing. *Phys. Rev. D*, **35**:2130, (1987).
- [24] J. Delorme, M. Ericson, A. Figureau, and C. Thevenet. *Ann. of Phys.*, **102**:273, (1976).
- [25] E.C. Achmedov, T.V. Tetereva, and R.A. Eramzhyan. *Sov. J. Nucl. Phys.*, **42**:40, (1985).
- [26] P. Christillin, M. Rosa-Clot, and S. Servadio. *Nucl. Phys.*, **A345**:331, (1980).
- [27] D.S. Armstrong, S. Ahmad, R.A. Burnham, T.P. Gorrings, M.D. Hasinoff, A.J. Larabee, C.E. Walthan, G. Azuelos, J.A. Macdonald, T. Numao, J-M. Poutissou, M. Blecher, D.H. Wright, E.T.H. Clifford, J. Summhammer, P. Depommier, R. Poutissou, and H. Mes. *Physical Review C*, **43**:1425, (1991).
- [28] R.S. Henderson, R.J. Dawson, M.D. Hasinoff, G. Azuelos, S. Ahmad, A. Serna-Angel, M. Blecher, T.P. Gorrings, B.C. Robertson, and D.H. Wright. *IEEE Transactions on Nuclear Science*, **37**:1116, (1990).
- [29] P. Bennett, M. Blecher, R. Chan, S. Daviel, M. Hasinoff, S. Ko, R. Poutissou, D. Sample, and D. Wright. *IEEE Transactions on Nuclear Science*, **37**:1200, (1990).
- [30] S. Ahmad et. al. *Nuclear Instruments and Methods*, **A286**:76, (1989).
- [31] S. Bird, R.G. Findlay, and A.A. Raffler. *Nuclear Instruments and Methods*, **166**:155, (1979).
- [32] E.W. Blackmore, D.A. Bryman, J.V. Cresswell, J. Doornbos, K.L. Erdman, J.A. Macdonald, R.M. Pearce, R.L. Poirier, J.M. Poutissou, J. Spuller, and G. Waters. *Nucl. Instrum. Methods*, **234**:235, (1985).
- [33] D.H. Wright *et al.* Triumf radiative muon capture facility. (1991). To be submitted to *Nuclear Instruments and Methods*.

- [34] J.P. Perroud, A. Perrenoud, J.C. Alder, B. Gabioud, C. Joseph, J.F. Loude, N. Morel, M.T. Tran, E. Winklemann, H. Von Fellenberg, G. Strassner, P. Truol, W. Dahme, H. Panke, and D. Renker. *Nucl. Phys.*, **A453**:542, (1986).
- [35] T. Suzuki, D.F. Measday, and J.P. Roalsvig. *Phys. Rev. C*, **35**:2212, (1987).
- [36] P. Hanggi, R.D. Viollier, U. Raff, and K. Alder. *Phys. Lett.*, **51B**:119, (1974).
- [37] H. Primakoff. *Rev. Mod. Phys.*, **31**:802, (1959).
- [38] H.P.C. Rood, A.F. Yano, and F.B. Yano. *Nucl. Phys.*, **A228**:333, (1974).
- [39] R.D. Hart, C.R. Cox, G.W. Dodson, M. Eckhause, J.R. Kane, M.S. Pandey, A.M. Rushton, R.T. Siegel, and R.E. Welsh. *Phys. Rev. Lett.*, **39**:399, (1977).
- [40] R.D. Hart. *Measurement of Radiative Muon Capture in Calcium*. PhD thesis, College of William and Mary, (1987). unpublished.
- [41] A. Frischknecht, W. Stehling, G. Strassner, P. Truol, J.C. Alder, C. Joseph, J.F. Loude, J.P. Perroud, D. Ruegger, M.T. Tran, W. Dahme, H. Panke, and R. Kopp. *Phys. Rev.*, **C32**:1506, (1985).
- [42] C.J. Virtue. *Photon Asymmetry in Radiative Muon Capture on Calcium*. PhD thesis, University of British Columbia, (1987). unpublished.
- [43] M. Dobeli. *Radiative Muon Capture Yield in Nuclei*. PhD thesis, University of Zurich, (1987). unpublished.
- [44] D.S. Armstrong. *Radiative Muon Capture on Carbon, Oxygen and Calcium*. PhD thesis, University of British Columbia, (1988). unpublished.
- [45] A. Frischknecht, W. Stehling, G. Strassner, P. Truol, J.C. Alder, C. Joseph, J.F. Loude, J.P. Perroud, D. Ruegger, M.T. Tran, W. Dahme, H. Panke, and R. Kopp. *Phys. Rev. C*, **38**:1996, (1988).
- [46] H.C. Chiang, E. Oset, and P. Fernández de Córdoba. *Nucl. Phys.*, **A510**:591, (1990).

VITAE

Name: Alvaro Serna

Date of Birth: November 4, 1954

Education: Ph.D. Physics, Oct. 1991
Virginia Polytechnic Institute and State
University, Blacksburg, VA

M.S. Physics, June 1982
Hunter College of the City University of New
York, New York, NY

B.S. Physics, Dec. 1978
Universidad de Antioquia, Medellin, Colombia

Address: Departamento de Fisica
Universidad Tecnologica de Pereira
Pereira, Colombia S.A.